JOURNAL OF CASTING
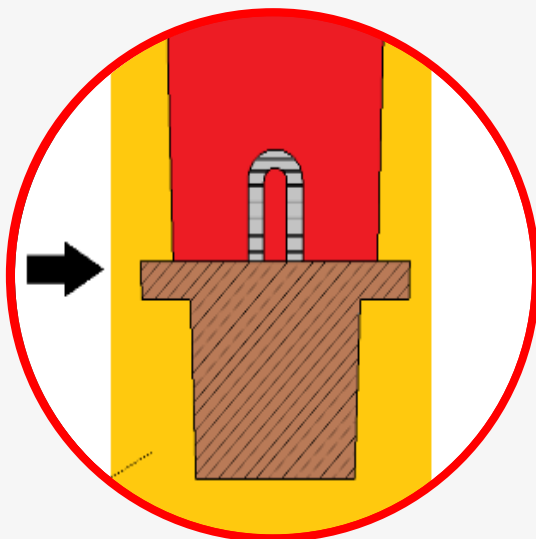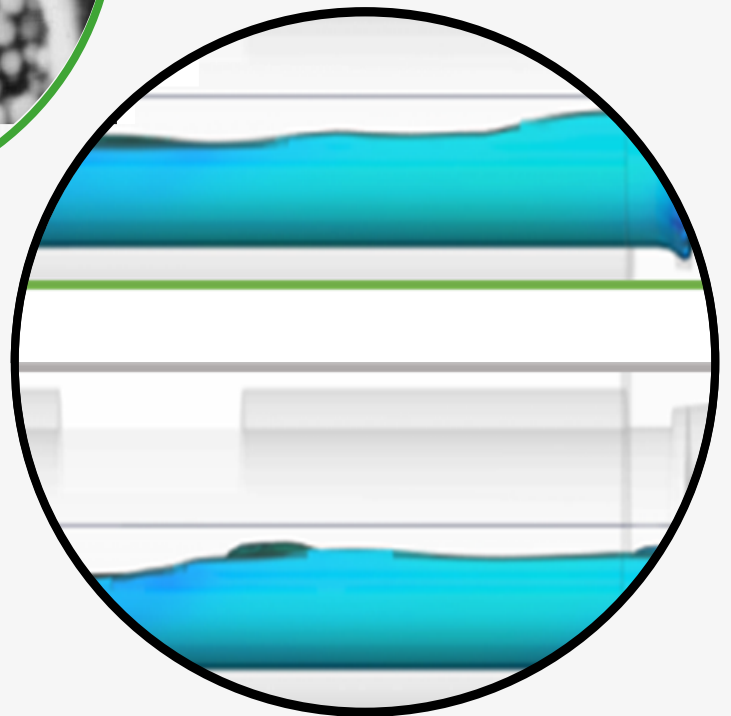## & MATERIALS ENGINEERING

AGH UNIVERSITY OF SCIENCE AND TECHNOLOGY
FACULTY OF FOUNDRY ENGINEERING

JcME

Contents

Optimization of Ladle Tilting Speed for Preventing Temperature Drops in the Die Casting Process

Haru Ando[a]*, Daichi Minamide[a], Yuto Takagi[a], Ken'ichi Yano[a], Naoto Nakamura[b], Masahiro Sano[b], Takahiro Aoki[b], Yasunori Nemoto[c]

[a] Mie University, Faculty of Engineering, Department of Mechanical Engineering, 1577 Kurimamachiya-cho, Tsu, Mie, Japan
[b] Yamaha Motor Co Ltd, 2500 Shingai, Iwata-city, Shizuoka, Japan
[c] Flow Science Japan, Inc. Motoasakusa MN Bid.7F, 1-6-13, Motoasakusa, Taito-ku, Tokyo, Japan
*e-mail: yanolab@robot.mach.mie-u.ac.jp

Abstract

In die casting, molten metal poured into a shot sleeve is pressed into a mold by a plunger at high speed. The temperature of the metal drops significantly while it is being poured from the ladle to the shot sleeve, resulting in casting defects such as misrun flow lines. Although it is important to control the temperature at all stages of the process, a method for minimizing temperature loss has not yet been clarified to date. In this study, the cause of the temperature drop in the shot sleeve was clarified, and a method of optimizing the ladle tilting speed was proposed to prevent temperature drop. First, experiments were conducted to measure the decrease in metal temperature in the sleeve during pouring. These experiments revealed that the metal cools significantly from the moment it touches the shot sleeve. Therefore, the time from the first contact between the shot sleeve and the metal to the start of pouring was set as the objective function. A genetic algorithm was then used to derive the optimal ladle tilting speed pattern to suppress the temperature drop. This analysis confirmed that the metal was poured without flowing out or running ahead and that the immediate liquid level vibration after pouring was suppressed, thus ensuring stable pouring.

1. INTRODUCTION TO THE SUBJECT AND PURPOSE OF THE RESEARCH

In die casting, when the casting temperature is too low, the flowability of the product is reduced, and casting defects such as misrun and flow line occur [1]. The problem is that the temperature of the molten metal drops significantly while it is flowing from the ladle to the shot sleeve. Therefore, a method to minimize the temperature drop at the stage before injection is necessary [2, 3].

One solution to this casting problem is to raise the temperature of the metal before injection it. However, increasing the thermal load on the shot sleeve causes cracks and shortens the life of the shot sleeve [4, 5].

A different solution is to fill the mold more quickly. To do so, the pouring speed of the ladle and the ejection speed of the plunger must be increased [6]. However, inadvertent pouring requires a waiting time for the molten metal surface in the sleeve to become static. During this time, the temperature will drop more [7].

In this research, we clarify the cause of the temperature drop when metal is poured into the shot sleeve during die casting. We then propose a pouring control input that can suppress the temperature drop during the pour and quickly proceed to the injection process. Finally, we show the effectiveness of the proposed method by comparing the derived control input with the control input used in the casting process by CFD simulation.

2. HEAT TRANSFER COEFFICIENT IDENTIFICATION FOR POURING MODEL

We conducted an experiment to measure the temperature of metal during pouring. In this research, we used a die casting machine (Shibaura Machine Co., Ltd DC135J-T). The sleeve, made of SKD61, has an inner diameter of 60 mm and a length

of 200 mm. The metal is an aluminum alloy (JIS-ADC12) with an initial temperature of 690°C and a casting weight of 0.71 kg (sleeve filling rate: 42.0%). The material properties of JIS-ADC12 are shown in Table 1. The tip of the ladle is placed 30 mm above the pouring hole of the shot sleeve and tilted to the sleeve at an angle of 45 deg.

Table 1
The material properties of JIS-ADC12

Properties	Values
Liquidus temperature	598°C
Solidus temperature	513°C
Density	2467 kg/m³
Viscosity	0.00145 Pa·s

We installed one sheath thermocouple in the ladle and six in the shot sleeve to measure the metal temperature during pouring. The locations of the thermocouples in the sleeve are shown in Figure 1. The top parts of the sleeve, in order from shortest to longest from the pouring hole, are labeled No. 1, No. 2, and No. 3, and the bottom parts are No. 4, No. 5, and No. 6. Figure 2 shows the temperatures from the start of pouring. The start time is when the thermocouple first measures the temperature in the shot sleeve.
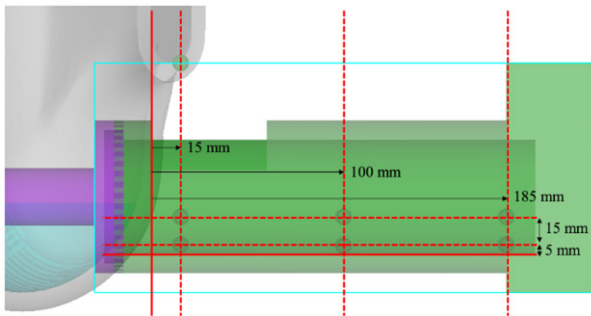

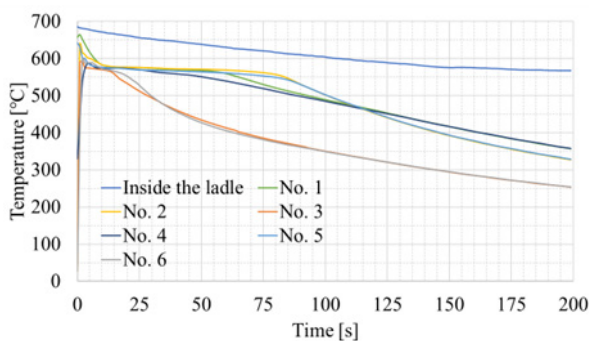**Fig. 1.** Temperature measurement positions inside the shot sleeve

Fig. 2. Molten metal temperatures

In Figure 2, the first curve shows the time-series temperature data at the measurement points set in the ladle, and the other curves are temperature data of molten metal at the measurement points shown in Figure 1. The metal temperature in the ladle at the start of pouring is almost the same as the initial temperature. Therefore, it is assumed that the

thermal diffusion from the molten metal to the air is very small during the conveyance and the tilting of the ladle.

Although the temperature at the first measurement point in the shot sleeve is close to the initial temperature, the temperature drops significantly and rapidly while the metal is being poured. After the completion of pouring, the temperature decreases slowly. This indicates that the heat transfer to the shot sleeve accounts for most of the temperature drop during pouring.

We used *FLOW-3D* from Flow Science, Inc. for CFD analysis. To construct the CFD pouring model, we needed to define the heat transfer coefficient between the metal and the shot sleeve using the experimental results. At this point, due to the time required for CFD simulation, we simulated the pouring model for 20 s from the start of tilting. In the simulation model, measurement points are set at the same six locations in the shot sleeve as in Figure 1.

Figure 2 shows that the time when the temperature peaks differs from point to point. It is assumed that this is due to the response delay of the thermocouples. Therefore, we compared the simulation results with the experimental results after the time when the peak temperature was reached, and adopted the heat transfer coefficient of the shot sleeve that shows the most similar temperature history. The value of Y is set to evaluate the similarity between the simulation results and the experimental results.

$$Y = \sum_{(i=1)}^{6} D_i \tag{1}$$

$$D_i = \sum_{(j=t_p)}^{20} (T_{ije} - T_{ija})^2 (j = t_p, \ t_p + 1, \dots, \ 20) \tag{2}$$

Here, i is number of the six measurement points shown in Figure 1, and j is the time t_p after the peak value. For the timeline of the experiment and the simulation, $t = 0$ s is the time when the temperature of the metal is first measured at any of the measurement points. For each measurement point, the residual sum of squares D_i between T_{ija} [°C] (the temperature calculated from simulation) and T_{ije} [°C] (the temperature calculated from simulation) is calculated. Then, the sum of D_i values for the six measurement points is defined as the evaluation value Y. We searched for the heat transfer coefficient with the minimum value of Y by using the golden section method. For the sleeve heat transfer coefficient, the search range is 0 to 2500 W/(m² · K) [8, 9].

3. TEMPERATURE DECREASE FACTOR ANALYSIS

From Equations (3) and (4), equations of heat transfer quantity, Q, the heat transfer quantity [W] is derived using h, the heat transfer coefficient [W/(m² · K)], and its value fluctuates greatly depending on the area of fluid–solid contact A [m²] and time t [s]. Here, T_a and T_w are the temperatures of objects in different phases.

$$Q = \int q \cdot A(t) \cdot dt \tag{3}$$
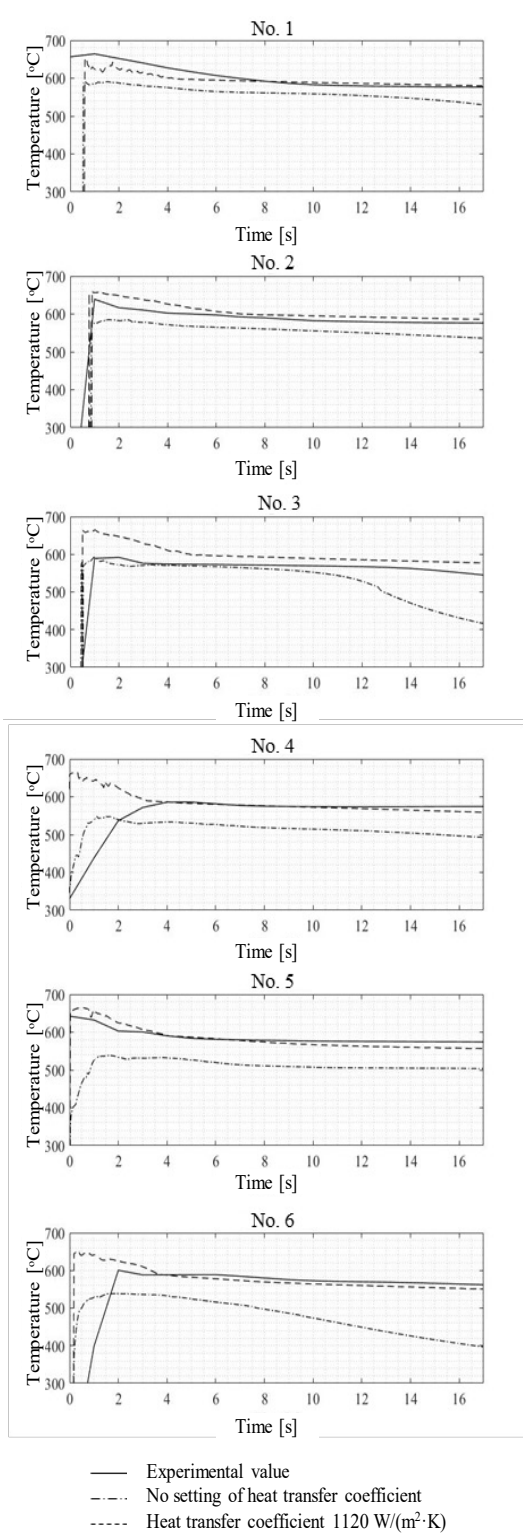
$$q = h(T_a - T_w) \tag{4}$$

Fig. 3. Temperature comparison between experiment and CFD simulation

Figure 3 compares the simulation results and the experimental results using the obtained optimum heat transfer coefficient of 1120 W/(m² · K). In the case of simulation without setting the heat transfer coefficient, the thermal diffusivity is estimated from the thermal conductivity. From Figure 3, it can be confirmed that the simulation results using the derived heat transfer coefficient are sufficiently similar to the metal temperatures measured in the experiment.

Therefore, the CFD simulation of the pouring model is performed using the derived heat transfer coefficient 1120[W/(m² · K). From the experimental results shown in Figure 3, it can be inferred that the heat transfer to the shot sleeve is much more dominant than that to the air in the temperature drop of the metal. To investigate the cause of the temperature drop, we performed CFD simulations using several tilt patterns. We then analyzed the molten metal near the inner surface of the shot sleeve, where temperature changes are large, focusing on the contact time and area with the shot sleeve. From the results, we searched for ways to improve the temperature drop. The following equation is the definition of the contact time Δt [s] between the inner surface of the sleeve and the metal. Δt is the difference between t_{first} (the time when the metal first touches the sleeve) and t_{fin} (the time when the pouring is completed).

$$\Delta t = t_{fin} - t_{first} \tag{5}$$

$$t_{fin} = \left\{ t \left| \begin{array}{c} \left| h_{|t=t,...,t_{end}} \right| < h_{max} \\ t > t_{first} \end{array} \right. \right\} \tag{6}$$

At the pouring completion time t_{fin} the molten metal surface must be in a static state. To determine this, t_{fin} is defined as the time when the maximum height h [m] of the molten metal surface converges to an arbitrary height h_{max} [m] or less. In this research, h_{max} is defined as the height of the metal surface at the time of static flow +10%.

The pseudo contact area of the metal with the inner surface of the shot sleeve is defined as the number of cells into which the metal flows. Figure 4 shows the relationships among the contact time and area of the metal with the inner surface of the shot sleeve and the average temperature of the metal at the time of pouring completion, obtained by CFD simulation.

As shown in Figure 4, the temperature drop depends strongly on the amount of time that the metal is in contact with the inner surface of the sleeve. This is because the contact area increases and decreases instantaneously and is not constant, so the effect on the temperature drop is small. Therefore, it is possible to suppress the drop by deriving a pouring control input that can shorten the contact time so that it quickly shifts to the injection process. In this research, we used the tilting speed input as the pouring control input and derived it by genetic algorithm (GA) optimization.
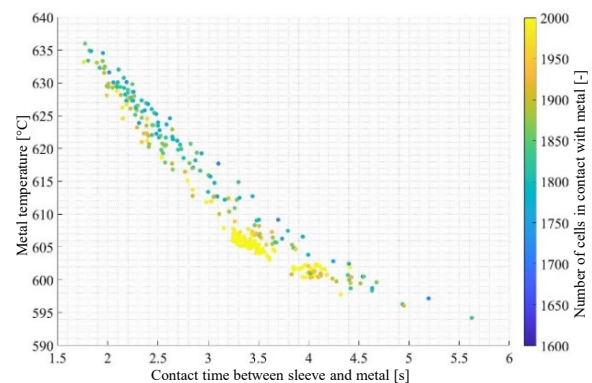

Fig. 4. Relationship between temperature drop and heat outflow to shot sleeve

4. TILTING SPEED INPUT OPTIMIZATION TO EVALUATE TEMPERATURE DROP OVER THE ENTIRE SETTABLE RANGE

The design variables of the optimization used in this research are shown in Figure 5. In the pouring system of the target die casting machine, the tilting speed is set using two speed parameters.
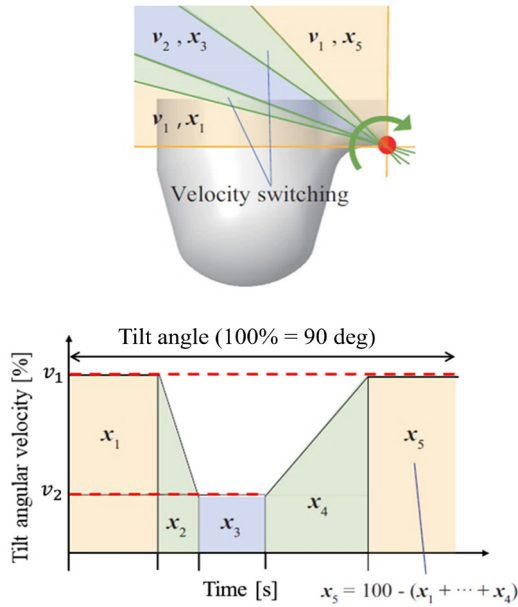

Fig. 5. Definitions of design variables for tilting speed

The parameters of the tilting speed are v_1 and v_2 [%], respectively. Due to the constraints of the die casting machine, the tilting speed input for the ladle is given in three steps, varying in the order of v_1 and v_2. These parameters are each set as a percentage of the maximum frequency of the inverter in the ladle tilt actuator, and the unit is percent. The speed parameter is temporarily denoted as [%]. If the actual tipping speed of the ladle is [rad/s], it can be converted as shown in Equation (7) from the experiment conducted by Kanazawa in this laboratory [10].

$$v' = 1.24v + 0.20 \qquad (7)$$

Then, the timing of speed switching is expressed as the amount of rotation x_1, x_2, x_3, x_4 [%] in each speed interval, taking the percentage of the total rotation of the tilt. The above six variables are defined, and the simulation is carried out until 3 s after the end of the tilt.

From the above, the contact time between the inner surface of the sleeve and the molten metal was set as an alternative evaluation value to suppress the temperature drop. Then, the tilting speed input that suppresses the temperature drop is obtained by GA optimization. The evaluation functions are shown in Equations (5) and (6). t_{fin} is the time when the area of the fluid touching the inspection surface (hereinafter referred to as flow surface area) [m²] at height h_{max} becomes less than the threshold value. As shown in Figure 6, the flow surface area increases and decreases continuously

during the pouring process due to the waves returning inside the shot sleeve. Therefore, t_{fin} is determined only when the flow surface area does not exceed the threshold value at any subsequent time.
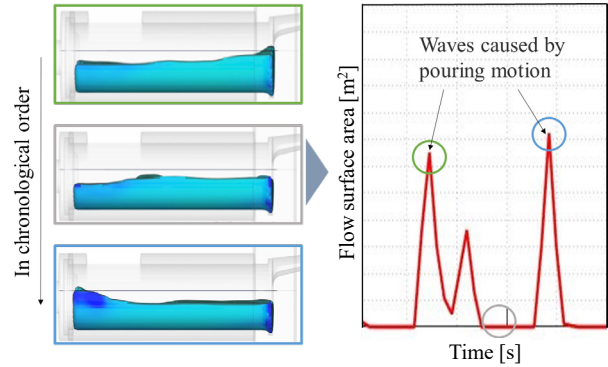
Fig. 6. Determination of pouring completion time

In this research, the threshold value is set to $3.0 \cdot 10^{-6}$ m² to account for calculation errors. Individuals whose liquid level oscillation does not stop by the end of the simulation are excluded from the solution.

Another constraint in the optimization was that we also excluded from the solution any individuals for which forerunning of metal or outflow outside the pouring hole of the shot sleeve was confirmed. Forerunning is a phenomenon in which the molten metal flowing into the product mold section solidifies before injection, and fragments of solidified metal flow into the inside of the product with molten metal. This phenomenon decreases product quality. In addition, if molten metal flows out of the shot sleeve pouring hole, there is a risk of deterioration in yield and a loss of safety. These two points are set as constraints on the feasibility. The location of the inspection surface is shown in Figure 7. In Figure 7a, forerunning has occurred if molten metal flows into the inspection surface installed at the sprue connected to the mold at the pouring process. In Figure 7b, an inspection surface is placed around the shot sleeve pouring hole to check for molten metal outflow.
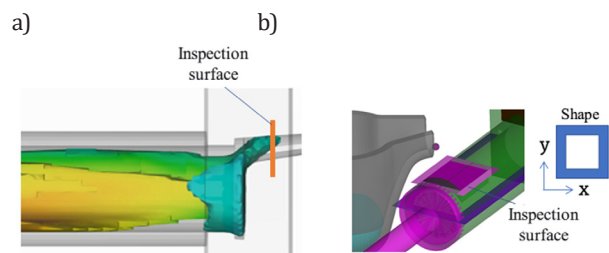
Fig. 7. The location of the inspection surface: a) forerunning inspection surface; b) outflow inspection surface outside the shot sleeve

In both conditions, the individual is evaluated only when the flow surface area of the inspection surface stays below the threshold value until the end of the simulation. The threshold value is set to $3.0 \cdot 10^{-6}$ m² to account for calculation errors as well as the evaluation function.

Using the evaluation function and the constraints described above, we defined the optimization problem as follows.

Minimize:

$$J(v, x) \tag{8}$$

Subject to:

$$0.1 \le v_1, \ v_2 \le 100 \tag{9}$$

$$0.1 \le x_1, \ x_2, \ x_3, \ x_4 \le 100 \tag{10}$$

$$I_1(t) < F_{min1} \tag{11}$$

$$I_2(t) < F_{min2} \tag{12}$$

$$F_{min1}, \ F_{min2} = 3.0 \cdot 10^{-6} \tag{13}$$

The objective function J is Δt (the contact time between the inner surface of the sleeve and the molten metal), I_1 is the flow surface area of the inspection surface at the sprue, and I_2 is the flow surface area of the inspection surface around the sleeve pouring hole. The optimization problem is solved using a general GA, and the optimization parameters are shown in Table 2.

Table 2
Optimization parameters

Number of generations	6
Population	100
Elite number	20
Selection method	Tournament
Crossing method	REX

The optimization results are shown in Figures 8 and 9. A single point in these figures represents a single individual. Figure 8 shows the convergence of the solution tendency based on the number of generations and the evaluation value (the contact time between the shot sleeve and the molten metal) of each individual. Figure 9 shows the relationship between the evaluation value, the time of completion of tilting, and the average temperature at the completion of pouring.

The point in red in Figure 9 show the results of the simulation using the conventional tilting pattern.

Figure 8 shows that 14 of 100 individuals satisfied the conditions in the initial generation. This means that the range within which molten metal can be poured safely is small and that the search has been insufficient. Therefore, the parent individuals are not similar, and the results do not approach the optimal solution even if they are crossed. In addition, Figure 9 shows that child individuals tend to be generated in order to shorten the time until tilting stops, rather than the evaluation value. This is a result of the fact that the direction in which the solution population of the child individuals evolved varied due to the insufficient number of parent individuals, and therefore converged to a localized solution before reaching the optimal solution.

To improve the efficiency of the search for the optimal solution, we redefined the range of design variables. For this

purpose, we analyzed the tilting patterns of the individuals with excellent optimization solutions shown in Equations (8)–(13), and determined the range of design variables in which the tilting pattern that enables stable pouring is likely to exist.
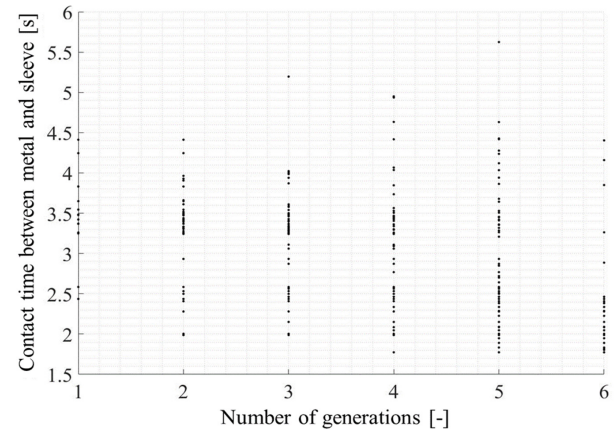
Fig. 8. Optimization convergence process
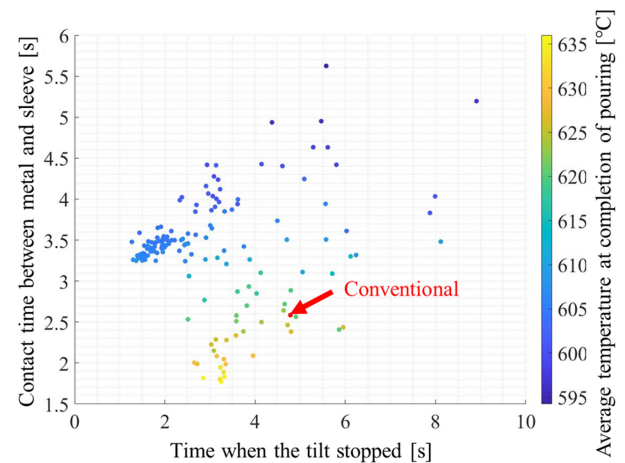
Fig. 9. Comparison of evaluation values of optimization results

5. OPTIMIZATION OF TILTING SPEED INPUT IN THE DESIGN DOMAIN CONSIDERING FEASIBILITY

Based on the optimization results described in Section 4, the relationship between the tilting speeds v_1, v_2 and the average temperature of the metal at the time of pouring completion is shown in Figure 10. Here, the x-marked solutions in the graph represent the individuals that were eliminated from the generation due to the constraint conditions, and the dots-marked group represents the individuals that were evaluated in the optimization algorithm.

From this result, it is clear that the constraint condition is rarely satisfied when both v_1 and v_2 are fast compared to other individuals. This is because the high-speed tilt causes a large disturbance in the metal behavior, thus preventing stable pouring. In the individual cases that satisfied the constraint conditions and were subject to evaluation, v_1 was relatively slow. Therefore, it is assumed that metal is poured without disturbing the liquid surface behavior because the speed slows down in the latter half of the ladle tilt when the metal starts to flow.
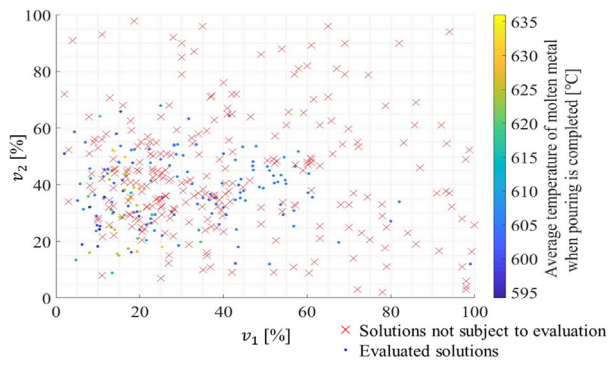
Fig. 10. Relationship between tilting speed and pouring feasibility

Based on this analysis, the range of design variables for the tilting speed was changed to the following equation in consideration of practicality.

$$0.1\% \leq v_1 \leq 30\% \tag{14}$$

$$0.1\% \leq v_2 \leq 70\% \tag{15}$$

The ladle tilting speed is optimized with the change in the range of design variables. The conditions of the optimization problem other than the tilting speed variables are in accordance with Equations (8), (10)–(13). Here, there are 50 individuals per generation, 7 generations, and 20 elite individual conservations. A general GA is used for optimization as in Section 4. The optimization results are shown in Figure 11 and Figure 12. In the figures, each point represents one individual, as in Section 3, and the red point in Figure 12 shows the result of the analysis using the conventional tilting pattern.
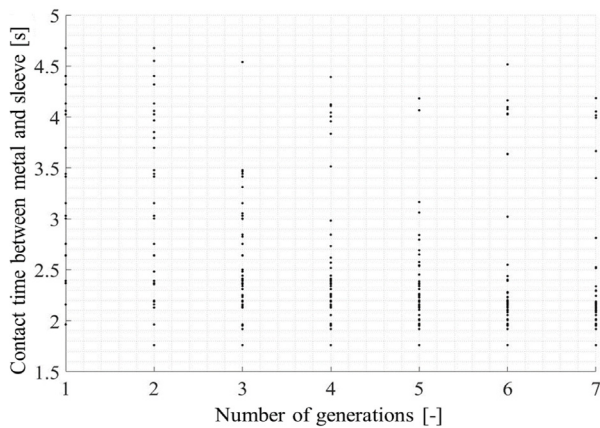

Fig. 11. Optimization convergence process

Figure 11 shows that 20 of 50 individuals satisfy the constraints in the initial generation. The percentage of feasible tilting speeds was higher than it was before the change in the range of design variables. In the second generation, 11 of 30 individuals satisfied the constraints, as did 17 of 30 in the third generation. Thus, the efficiency of the search for stable tilting speed input has been improved. From Figure 12, it can be confirmed that a solution group close to the optimum solution is formed without splitting the group. Here, we

focused on the fact that the evaluation is often poor in cases where tilting stops after only a short time. This is because the shot time lag tended to become longer because the metal was violently disturbed in the shot sleeve during pouring by high-speed tilting. The same phenomenon was observed in the previous research, which guarantees the reproducibility of the CFD simulation model in this research.
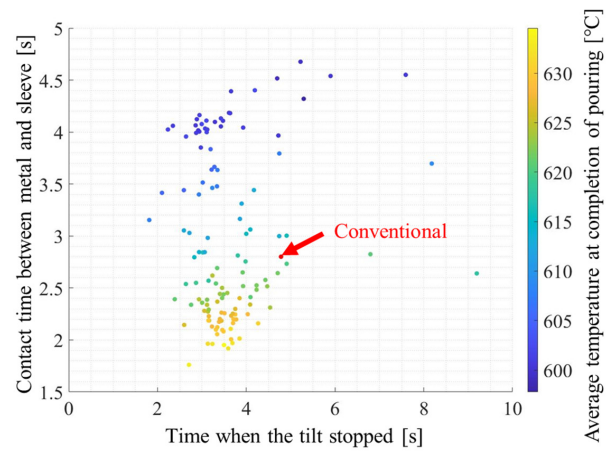
Fig. 12. Comparison of evaluation values of optimization results

The CFD simulation results of the pouring model with the optimized tilting speed input and the conventional input are shown below. Figure 13a shows the average temperature history of the metal, and Figure 13b compares the derived tilting speed input and the conventional tilting speed input used in actual die casting manufacturing.

The simulation results in Figure 13 show that the derived tilt pattern can suppress the temperature drop by 15.9°C compared to the conventional tilt pattern. The time to complete pouring was also shortened. In the design of the tilting speed input, it was clarified that the pouring could be completed while the liquid level of the metal was calm by using a high rotation speed for the first half of the ladle tilt and by extending the low-speed part in the second half.

a)

b)

Fig. 13. The CFD simulation results of the pouring model with the optimized tilting speed input and the conventional input: a) temperature history of the metal; b) tilting speed input

6. CONCLUSIONS AND SUMMARY

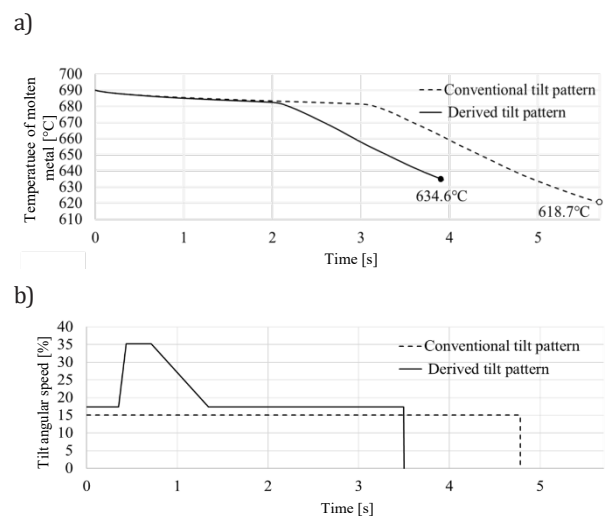In this research, we focused on the temperature drop during pouring in die casting and analyzed the factors in the drop using CFD simulation. The experiment to measure the decrease in metal temperature in the shot sleeve during pouring proved that the temperature decreases significantly from the moment the metal touches the sleeve. Therefore, the time from the first contact between the sleeve and the molten metal to the injection start time was set as the objective function, and the optimal ladle tilting speed pattern to suppress the temperature drop was derived using a genetic algorithm. The simulation confirmed that the derived tilting speed input did not cause metal to flow out or forerunning, and suppressed the turbulence of the metal surface immediately after pouring, thus ensuring stable pouring.

REFERENCES

[1]   Laukli H.I., Arnberg L. & Lohne O. (2005). Effects of grain refiner additions on the grain structures in HPDC A356 castings. *International Journal of Cast Metals Research*, 18(2), 65–72. Doi: https://doi.org/10.1179/136404605225022919.

[2]   Yu W., Cao Y., Guo Z. & Xiong S. (2016). Development and application of inverse heat transfer model between liquid metal and shot sleeve in high pressure die casting process under non-shooting condition. *China Foundry*, 13, 269–275. Doi: https://doi.org/10.1007/s41230-016-5137-4.

[3]   Sugihara T., Fujishiro M. & Maeda Y. (2019). Direct Observation and simulation of ladle pouring behaviour in die casting sleeve. *VI International Conference on Particle-Based Methods: fundamentals and applications, 28–30 October, Barcelona*. Barcelona: CINME, 610–618.

[4]   Vachhani H., Rathod M. & Shah R. (2019). Dissolution and erosion behavior of AISI H13 shot sleeve in high pressure die casting process. *Engineering Failure Analysis*, 101, 206–214. Doi: https://doi.org/10.1016/j.engfailanal.2019.02.021.

[5]   Abid D., Ktari A., Mellouli D., Gafsi N. & Haddar N. (2019). Failure analysis of shot–sleeves used in brass high pressure die–casting process. *Engineering Failure Analysis*, 104, 177–188. Doi: https://doi.org/10.1016/j.engfailanal.2019.05.038.

[6]   Korti A.I.N. & Abboudi S. (2017). Effects of shot sleeve filling on evolution of the free surface and solidification in the high-pressure die casting machine. *International Journal of Metalcasting*, 11(2), 223–239. Doi: https://doi.org/10.1007/s40962-016-0051-5.

[7]   Iwata Y., Dong S., Sugiyama Y. & Iwahori H. (2013). Effects of solidification behavior during filling on surface defects of aluminum alloy die casting. *Materials Transactions*, 54(10), 1944–1950. Doi: https://doi.org/10.2320/matertrans.F-M2013819.

[8]   Helenius R., Lohne O., Arnberg L. & Laukli H.I. (2005). The heat transfer during filling of a high-pressure die-casting shot sleeve. *Materials Science and Engineering: A*, 413–414, 52–55. Doi: https://doi.org/10.1016/j.msea.2005.08.166.

[9]   Yu W., Cao Y., Li X., Guo Z. & Xiong S. (2017). Determination of interfacial heat transfer behavior at the metal/shot sleeve of high pressure die casting process of AZ91D Alloy. *Journal of Materials Science & Technology*, 33(1), 52–58. Doi: https://doi.org/10.1016/j.jmst.2016.02.003.

[10] Kanazawa K. (2015). *Nonparametric shape optimization methods using parametric curves*. Graduate School. Mie University [Doctoral Dissertation].

The Optimization of a Numerical Steel Foundry Simulation Through a Characterization of the Thermal Properties of the Materials

Morgan Souêtre[a, b, c*], **Alexis Vaucheret**[a, b] (iD)**, Philippe Jacquet**[a, b] (iD)**, Jean-François Carton**[c] (iD)

[a] Université de Lyon, ECAM LaSalle, LabECAM, F-69005 Lyon, France
[b] Arts et Métiers Institute of Technology, LaBoMaP, HESAM Université, 71250 Cluny, France
[c] SAFE Metal, 1 Boulevard de la Boissonnette, 42110 Feurs, France
*e-mail: morgan.souetre@ecam.fr

Abstract

In many foundries, numerical simulation is used to determine the origins of different defects as this tool allows the acceleration of the design process. However, the databases provided by different software do not seem to tally with the actual properties of the material. In fact, every foundry uses a different grade of steel and varying mixtures of sand. An evaluation of the impact of different material properties showed the importance of measuring every physical property to improve the database of the software. Following this, an experiment was conducted to evaluate the gap between numerical simulations and the results obtained through experimentation. This experiment, called thermal analysis, consists in measuring the solidification and cooling of a cylinder filled with liquid steel. After the calculation of the steel properties and a simulation with real experimental parameters, a comparison between each cooling curve was realized. This comparison shows that the calculated properties provide a simulated cooling curve which is closer to the experimental curve than the properties in the original database. We did not explore all of the metal properties in this study, but the modification of the sand properties was explored, together with the thermal conductivity of the steel and sand. These other measurements will be obtained in a future study.

1. INTRODUCTION

In the foundry process, high temperature liquid metal is poured into a mold before it cools and solidifies. The solidification of molten metal induces contraction and this contraction takes place from outside to inside, which can lead to a lack of metal in the center of the part, in a process known as shrinkage. Numerical foundry simulation is used to predict manufacturing defects, especially shrinkages. It is possible to anticipate and eliminate shrinkage defects by adding a sacrificial element called risers. Risers are cylindrical parts that concentrate the shrinkage and are removed from the final product to make the cast free of any defects. Some basic rules exist which govern the design of foundry parts [1, 2] with handmade calculation, but the more complex the part is, the more complex the calculations. To reduce the time needed for these calculations and increase their accuracy, foundries use numerical simulation. Moreover, these tools are able to calculate filling, solidification, and cooling.

Commercial software like Magma®, NovaFlow&Solid® (NFS), TherCast®, ProCast®, Flow3D® or QuickCast® make the designer's work easier, faster, and more precise. These tools have become essential, but require accurate entry data [2, 3]:

- process parameters: initial temperature of metal and mold, type of ladle, height of the ladle, dimension of the metal jet, etc.
- material parameters: chemical composition, density, specific heat, latent heat, conductivity, viscosity, etc.
- the measurement of physical properties is a very complex process for a steel foundry due to the high temperatures of processing (up to 1700°C). There is also a lack of information existing in databases [4]. Without accurate data, it is unthinkable that good simulation results can be obtained.

Software is available which includes a database containing physical properties of some metals and mold material. The user choses the closest material to its own, but this material does not usually match the requirements as the composition

could be slightly different and the specific process of the user might affect the real physical properties. Sometimes differences between reality and simulation are observed and as references [5] and [6] show, substituting material properties included in the original database with measured properties can really improve the results.

2. PRELIMINARY NUMERICAL STUDY

The first step of this work was to set the limitations of the NFS software. Firstly, a mesh study was conducted to reduce the influence of numerical parameters on thermal simulation results. Secondly, a sensitivity study was performed to evaluate the impact of material properties on simulation results. The second point will eventually help to highlight the prevalence of some properties in comparison to others.

For these two studies, the geometry used is a cube with sides of 50 mm with a virtual thermocouple placed in its center. The simulations were realized between 1600°C (standard temperature for low-alloyed steel casting) and 500°C; we will mainly analyze solidification in this paper. The steel grade used is "G20Mn5", a standard alloy in industrial foundry. The cube is surrounded by green sand in a layer of 40mm thick, where it serves as the molding material.

2.1. Meshing

NFS is based on a finite volume method meshing method. The software offers two methods to define the meshing that can be applied automatically: selecting the mesh count or choose the mesh size in mm. There is no way to select another parameter like local refinement.

To reduce the influence of meshing on the simulation results, a preliminary study on the cooling curve of the cube was carried out. The simulations were realized by varying the mesh size from the high size of 5 mm to the low size of 0.5 mm. This allows to determine the minimum size of meshing to use for the simulations to follow.

Protocol

All parameters remained constant except the mesh size:

- metal: "G20Mn5",
- mold material: "green sand",
- start temperature: 1600°C,
- ending temperature: 500°C,
- mesh size: 5 mm, 2.5 mm, 1.5 mm, 1 mm, 0.75 mm, 0.5 mm.

After simulation, the shapes of the cooling curves will be compared to examine the time for total solidification and the simulation duration.

Results

The different cooling curves are presented in Figure 1. Concerning the influence of the mesh size, the impact is quite low and below 1mm, the results are equivalent.

When comparing the different simulation times in Table 1, it is observed that the time of simulation is dependent on the mesh size; for these reasons, it is necessary to do a simulation

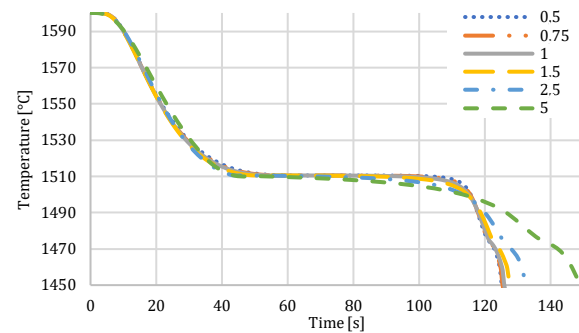with the roughest meshing, but with the consideration of the least influence on solidification time.

Fig. 1. Mesh study impact on the cooling curve

Table 1
Time of simulation by size of meshing

Mesh size [mm]	5	2.5	1.5	1	0.75	0.5
Simulation time [s]	1	11	90	1286	3555	29,500

This part shows that the mesh size has an impact on both solidification and simulation time. To obtain the lowest influence of the mesh on the result we need to refine it, but the simulation time grows as a consequence. That is why we need to choose a mesh size that offers limitation in simulation time, with little impact on the time of solidification. We will use a 1 mm mesh thereafter.

2.2. Sensitivity

Some results from the literature [7–9] have shown that physical properties do not have the same impact on the solidification time. In order to confirm this (or not) and to see the impact of some modifications, a number of simulations were completed using the cube described earlier.

Protocol

The reference simulation was done using "G20Mn5" steel grade and "Green sand" as the mold material from the NFS database. The simulations were done with 1 mm mesh size as determined in the previous section. For each property, five simulations have been realized, its value varying from 80% to 120% around the original value from NFS database with 10% steps, while the other properties were kept constant. For each calculation, the complete solidification of the cube was determined.

Results

The corresponding results are presented in Figure 2. At first, it seems that none of the properties were predominant: a variation of 10% of any of these properties involves a variation of approximately 5% on the solidification time. These results are valuable and close to the initial properties (more or less 20%) and if no coupled interaction between them exist. This means that for each of these properties, experimental measurements or calculation by means of software like ThermoCalc® or JMatPro® will be necessary to check if the accuracy of the NFS database properties.
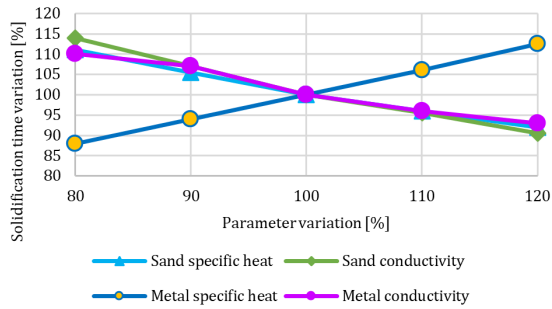
Fig. 2. Curve of time variation of the solidification of cube depending on the sensitivity of material

3. EXPERIMENTATION

The numerical study shows that exact properties are required to obtain good results. The exact chemical composition of the cast steel was measured by glow discharge optical emission spectroscopy (GDOES). A difference of composition between "G20Mn5" from NFS and cast steel (Tab. 2) is noticed.

Table 2
Steel grade composition [% weight]

Element	Fe	C	Mn	Si	Cr
Grade measured	98.47	0.31	0.81	0.41	0
Grade NFS	98	0.15	1.2	0.45	0.2

This difference is very important, firstly, the weight percentage of carbon of "G20Mn5" from the NFS database implies no peritectic transformation during solidification, contrary to the casted sample grade. Secondly, the liquidus and solidus are quite different and finally, each difference in composition could bring a modification of physical properties. It is for this reason that it was decided to determine most of them.

While analyzing the sand, it was found that the heat capacity curve of the silica sand (87.4% of green sand) [10] is different from the property given in the NFS database. As shown in Figure 3, the endothermic phase change of quartz-α into quartz-β (573°C) and the transformation of quartz into tridymite (≈870°C) and into crystobalite (≈1100°C) are not taken in account [11]. Water contained in the green sand, which induced high endothermic vaporization, was observed not to simulate and led to errors [12, 13].
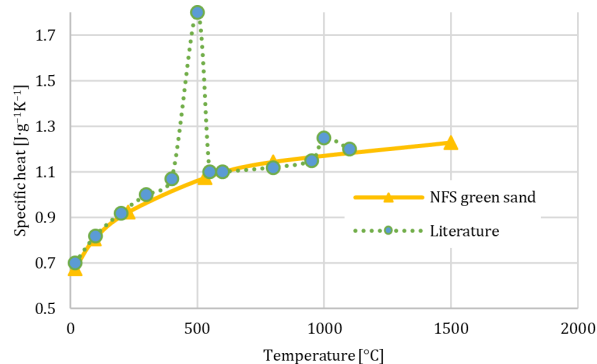

Fig. 3. Silica sand specific heat from literature [10] compared to NFS green sand

3.1. Property measurement and calculation

To obtain the physical properties, it is possible to measure each property based on temperature. However this requires expensive material and a lot of time. However, the properties of metal can be calculated with the use of its chemical composition calculated with the CALPHAD method [14]. This method is used for the calculation of properties thanks to the phase diagram [15]. The properties obtained seem to be suitable for improving the simulation results.

After the calculation of different properties using software such as JMatPro® and ThermoCalc®, for the composition given in Table 2, a difference between properties from the NFS database and the calculated properties were observed. The results given in Figure 4, for example, show a difference between the calculated density obtained by mens of the CALPHAD method and NFS database density. This difference seems to be low, but also exists in other properties: specific heat and latent heat.
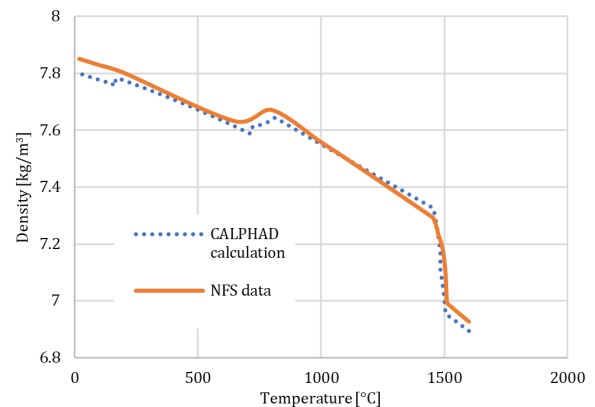
Fig. 4. Curve of density obtain by calculation compared to NFS database properties

The amount of water contained in the sand was measured to simulate its vaporization with the method of addition of specific heat around the water vaporization temperature (100°C) [12]. To obtain the amount of water, a precision scale is used to measure the loss of weight of the green sand after being dried between room temperature and 120°C. This measure gives us the weight percentage of water in the green sand, which resulted in approximately 4% for this study. With the use of this value and the water vaporization latent heat (2257 J · g⁻¹), the energy absorbed by this phase transformation for 1 g of green sand can be calculated:

$$2257 \cdot \frac{4}{100} = 90.28 \ \mathrm{J \cdot g^{-1}} \tag{1}$$

For comparison, the specific heat of the sand at 100°C is approximately 0.8 J · K⁻¹ · g⁻¹, which means that it needs around one hundred times more energy to increase the green sand temperature with 4% of humidity by 1°C at 100°C than it needs for the rest of the temperature range. To consider this phenomenon, this energy was added to the specific heat with a temperature range of 10°C from the vaporization temperature as had been observed in the literature [12].

3.2. Protocol

Physical experimentation

In order to control the improvements of the simulation due to the database modifications described previously, a specific trial based on a standard thermal analysis cup was developed. Thermal analysis is currently employed for the determination of the physical properties of steel or cast iron like liquidus and solidus [16, 17]. For simulation, the designed cylinder with a similar geometry to a standard thermal analysis bucket with a virtual thermocouple was placed in the same position to the real one in the experimental trials (Fig. 5).

Fig. 5. Design of a thermal analysis used for the study of steel properties

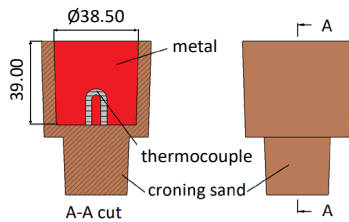Usually, for thermal analysis, experiments are conducted in air. The cup is placed on a support to facilitate filling: the cavity is filled with a ladle by the upper part. However, this generates lot of heat exchange by radiation, which is poorly simulated by NFS because this condition is rarely seen in foundry. Indeed, NFS only takes into account a fixed emissivity, when in reality, this property depends on the temperature and the state of the metal: liquid, solidified, clean or oxidized and depend on the surface state. That is why it was decided to cover the metal with a lid of green sand: just after the filling (directly in the cup), a lid is placed on top to close the mold. Furthermore, to study the impact of the green sand parameters, the sides of the thermal analysis bucket were cut, as in Figure 6, to remove the lateral part made of Croning sand, which is different from green sand. The lower part of the thermal analysis bucket was kept for practical reasons.
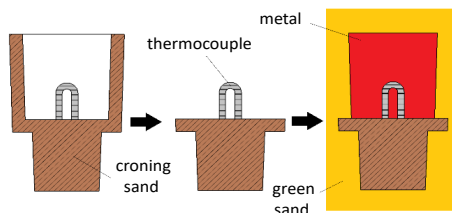

Fig. 6. Plan of cutting of sides of thermal analysis bucket

After cooling, the casts parts were weighed in order to carry out simulations with a precise amount of steel. This step is crucial because the time of solidification depends on the mass of the metal. Moreover, the starting temperature of the simulation is a key parameter; it is for this reason that the temperature of the alloy was directly measured in the crucible outside of the oven. It is necessary to subtract 40°C from the measured temperature to take into account the loss of heat due to the transportation of the crucible. The loss of heat has been the subject of a previous test campaign to measure it precisely.

Numerical experimentation

To compare the experimentations and simulations, the same cylinder was simulated, with the same mass of metal in it. A mesh size of 1 mm was chosen in accordance with the first experimentation and only the solidification and cooling of the metal was simulated, not the filling. For the simulation, Croning sand was not taken into account and it was replaced with green sand. Four different simulations were realized:

- standard grade: steel grade "G20Mn5" from the NFS database,
- standard grade exact composition: steel grade "G20Mn5" from NFS database with composition modified (measured by GDOES),
- calculate grade: exact composition and properties from the CALPHAD method,
- calculate grade + modified sand: exact composition and properties from CALPHAD method + sand with specific heat modified to take into account water vaporization.

4. RESULTS

As Figures 7 and 8 shown, the modification of metal properties changes the shape of the solidification curve whereas the modification of sand properties only modifies the speed of the cooling process. When observing the experimental curve, a difference in the shape at the beginning due to the process is observed: the mold is filled at room temperature whereas metal simulations are carried out at 1515°C.
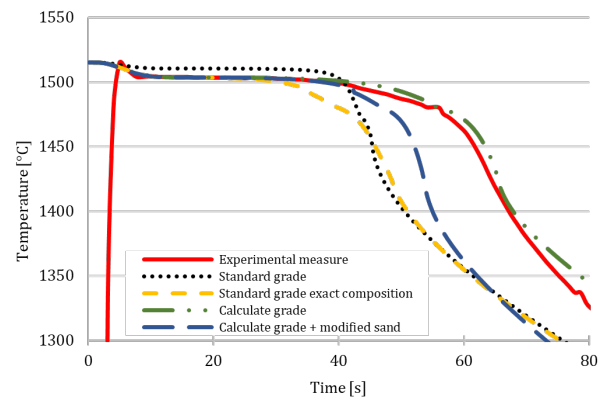

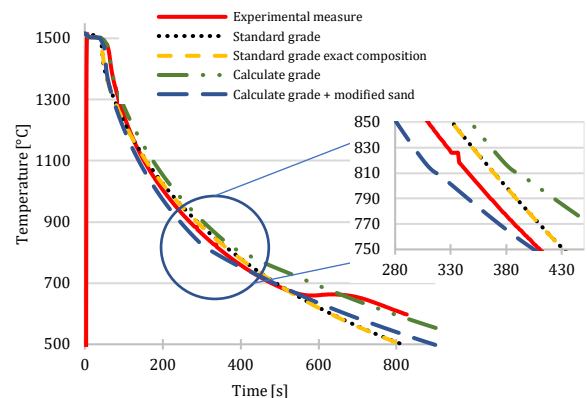**Fig. 7.** Solidification curve of experimentation and simulations

Fig. 8. Cooling curve of experimentation and simulation

Firstly, it is possible to see that the "Standard grade" has a change phase temperature different from the "Experimental measure". The liquidus temperature is also different. After modification of the chemical composition in the NFS database, the "Standard grade exact composition" change phase temperature seems similar to the "Experimental measure" but the solidification takes place too quickly. The "calculate grade" seem to be really close to the "Experimental measure", with the same solidus temperature and even the peritectic transformation at 1480°C observed. Unfortunately, changing the properties of sand (calculate grade + modified sand) leads to a worse match between the simulation and the experimental results. This was expected because of the heat absorption of water which is highly endothermic. The water vaporization absorbs a part of the heat and, as a result, the metal cools (and solidifies) faster. This means that for a better fitting between the simulation and the experiment, other parameters have to be taken into account, such as sand conductivity for example.

In Figure 8, the complete cooling curve is presented. The biggest difference between simulation and experimentation is the eutectoid transformation around 680°C. Indeed, NFS does not simulate this exothermic transformation. The use of properties calculated using data from the CALPHAD method ("calculated grade" and "calculated grade + sand modification") leads to a break in the slope around 800°C. This result is expected and is due to a solid/solid transformation ($\gamma \rightarrow \gamma + \alpha \rightarrow \alpha + Fe_3C$). This transformation is less visible on the experimental curve.

5. CONCLUSION

To improve the thermal simulation of a piece of casting simulation software (NovaFlow&Solid), metal properties in the database are modified. These properties are: composition, density, specific heat and latent heat. The impact on solidification and cooling of steel are studied; to estimate this impact, a thermal analysis experimentation has been used.

The first study (mesh size + sensitivity) showed the need to take all the physical properties (metal and sand) into account. The modification of steel's chemical composition in the NFS database leads to an improvement of the solidification temperature but did not change the solidification time. Improvement for future experiments can be obtained by modifying the physical properties with the use of the CALPHAD calculation. Nevertheless, the eutectoid transformation is still not observed on simulation curves. Future work will focus on the artificial implementation of exothermic heat during the eutectoid transformation (as was done for water vaporization) and experimental measurements of the thermal conductivity of steel and sand to obtain a more precise accuracy of the database regarding this property. Finally, a point to consider would be taking thermal resistance into account due to the presence of a layer of air between the metal and the mold [18].

Acknowledgments

REFERENCES

[1] Chvorinov N. (1940). Theorie Der Erstarrung Von Gußstücken. *Gießerei*, 27, 177–188.

[2] Wlodawer R. (1966). *Directional Solidification of Steel Castings.* London: Pergamon Press.

[3] Popielarski P. (2020). The Conditions for Application of Foundry Simulation Codes to Predict Casting Quality. *Terotechnology XI. Materials Research Proceedings*, 17, 23–30. Doi: https://doi.org/10.21741/9781644901038-4.

[4] Rappaz M. (2020). Does MCWASP Still Follow Moore's Law? Forty Years of Advances in Microstructure Modeling. *IOP Conference Series: Materials Science and Engineering*, Vol. 861. Doi: https://doi.org/10.1088/1757-899x/861/1/012001.

[5] Bernat Ł. & Popielarski P. (2020). Identification of Substitute Thermophysical Properties of Gypsum Mould. *Archives of Foundry Engineering*, 20(1), 5–8. Doi: https://doi.org/10.24425/Afe.2020.131274.

[6] Tiberto D. & Klotz U.E. (2012). Computer Simulation Applied to Jewellery Casting: Challenges, Results and Future Possibilities. *Materials Science and Engineering*, 33. Doi: https://doi.org/10.1088/1757-899x/33/1/012008.

[7] Mills K.C. & Lee. P.D. (2001). Thermophysical Property Requirements for Modelling of High Temperature Processes. *Proceedings: First International Symposium on Microgravity Research and Applications in Physical Sciences and Biotechnology*, 10–15 September 2000, Sorrento, Italy, SP-454 , 555–564.

[8] Kavicka F. & Stetina J. (2000). The Influence of Thermophysical Properties of Steels on the Numerical Simulation of a Concasting Process. In: Brebbia C.A. & Power H. (Eds.), *Boundary Elements XXII*, 243–252.

[9] Prikhod'ko O.G., Deev V.B., Prusov E.S. & Kutsenko A.I. (2020). Influence of Thermophysical Characteristics of Alloy and Mold Material on Casting Solidification Rate. *Steel in Translation*, 50, 296–302. Doi: https://doi.org/10.3103/S0967091220050095.

[10] Svildró J., Diószegi A. & Svidró J.T. (2020). The Origin of Thermal Expansion Differences in Various Size Fractions of Silica Sand. *International Journal of Cast Metals Research.* Doi: https://doi.org/10.1080/13640461.2020.1838078.

[11] Kowalski J. (2010). Thermal Aspects of Temperature Transformations in Silica Sand. *Archives of Foundry Engineering*, 10(3), 111–114.

[12] Ignaszak Z. & Popielarski P. (2015). Effective Modeling of Phenomena in Over-Moisture Zone Existing in Porous Sand Mould using the Simplified Simulation Systems Applied in Foundry. *Defect and Diffusion Forum*, 365, 200–206. Doi: https://doi.org/10.4028/www.scientific.net/ddf.365.200.

[13] Ignaszak Z. & Popielarski P. (2016). Identification of the Moisture Distribution in the Intensively Heated Porous Sand Mould. *Defect and Diffusion Forum*, 367, 121–129. Doi: https://doi.org/10.4028/www.scientific.net/ddf.367.121.

[14] Kaufman L. & Nesor H. (1978). Coupled Phase Diagrams and Thermochemical Data for Transition Metal Binary Systems – I. *Calphad*, 2(1), 55–80. Doi: https://doi.org/10.1016/0364-5916-(78)90005-6 .

[15] Dantzig J.A. & Rappaz M. (2016). *Solidification,* 2nd Edition, Lausanne: EPFL Press.

[16] Hecht M. (1986). L'analyse thermique en fonderie de fonte. *Centre Technique des Industries de la Fonderie.* Edition Techniques Des Industries De La Fonderie, Paris.

[17] Djurdevic M.B. (2021). Application of Thermal Analysis in Ferrous and Non Ferrous Foundries. *Metallurgical and Materials Engineering*, 27(4), 457–471. Doi: https://doi.org/10.30544/673.

[18] Abouchadi H. (2002). *Mise au point de tests expérimentaux pour validation thermomécanique du procédé de moulage des aciers.* PhD Thesis. Ecole Nationale D'arts Et Métiers, Paris.

The Formation, Properties and Use of Dispersed Iron-Graphite Metallurgical Waste

Leonid Dan[a]* [iD], Vladimir Maslov[b], Larysa Trofimova[b] [iD], Grzegorz Cios[a] [iD]

[a] AGH University of Science and Technology, Academic Centre for Materials and Nanotechnology, al. A. Mickiewicza 30, 30-059, Krakow, Poland
[b] Priazovskyi State Technical University, Faculty of Metallurgy, Dmytro Yavornytsky, Av. 19, 49005, Dnipro, Ukraine
e-mail: danleonid.alex@gmail.com

Abstract

Dispersed wastes containing graphite, iron, and its oxides, getting into the air and accumulating in landfills, cause serious harm to human health and the environment. Moreover, even if the issue of the localization of these wastes has been solved successfully, their disposal has not yet been fully organized. In the present study, a systematic analysis of the dispersed iron-graphite waste (IGW) conditions for the formation at metallurgical enterprises, their structure, and their properties were carried out. In this case, special attention is focused on the electrophysical properties: specific saturation magnetization and volume resistivity. The presence of magnetic properties in IGW, combined with low electrical resistivity, makes IGW a promising and inexpensive raw material for obtaining cheap composite materials with radio shielding and radio absorbing properties in the microwave range. As a result of the research, effective ways of improving the magnetic properties of IGW by high-temperature treatment were obtained. The practical result of the research was the development and implementation of a technological scheme of dispersed IGW complex processing, which makes it possible to solve a twofold task – to exclude the ingress of iron-graphite wastes into the environment and to obtain a cheap material for protection against microwave radiation.

Keywords:

1. INTRODUCTION

The metallurgical industry occupies one of the leading places regarding the degree of negative environmental impact. The reduction of greenhouse gas emissions by metallurgical enterprises is one of the main problems which the efforts of scientists and engineers are currently focused [1]. At the same time, attention is being drawn to the fact that in the production of 1 ton of cast iron, up to 600 g of waste containing graphite and iron oxides – iron-graphite waste is emitted [2]. Global practices show that iron-graphite waste can be used in metallurgy and in many other industries [3–7]. Technologies that make it possible to extract only the graphite component of IGW prevail, while the remainder is turned into waste again. This is unacceptable from an environmental point of view and irrational from the economic perspective because, in addition to graphite, the composition of IGW includes valuable components – iron oxides and metallic iron.

Therefore, the solution to issues related to the search for new IGW complex processing technologies, expanding the scope of their application, meets, on the one hand, the requirements of environmental protection and, on the other hand, allows for the more efficient use of valuable raw materials.

2. CONDITIONS FOR THE FORMATION OF DISPERSED IGW AT METALLURGICAL ENTERPRISES

Iron-graphite wastes have different compositions, structures, and properties depending on the formation at metallurgical enterprises.

Dispersed IGW is essentially graphite dust (kish graphite together with the tiniest splashes of cast iron and slag released into the atmosphere during the pouring and desulphurization of liquid iron), which is collected by aspiration systems.

The formation of graphite dust is explained [8, 9] by the dissolution of cementite in austenite and its dissociation into Fe and C as the cast iron cools when it leaves the furnace. In this case, the solution of carbon in iron becomes supersaturated,

which leads to the formation of graphite nuclei and their further intensive growth. Furthermore, the density of graphite is 2–2.5 times less than the density of metal, so the metal tends to push the plates to the surface, and since the metal does not wet them, they are freely blown away from the surface by the gas flow. In this regard, graphite dust is formed with any increase in the open (specific) surface of the metal, for example, during overflows or during its transportation through chutes. The solubility of carbon in an iron-carbon melt (Eq. (1)) and in real cast iron containing silicon and other elements (Eq. (2)) is expressed, respectively, by temperature dependences based on empirical formulas [8]:

$$C_1' = 1.30 + 2.57^{-3}t \tag{1}$$

$$C_1 = 1.27 + 2.57 \cdot 10^{-3}t - 0.34\text{Si} \tag{2}$$

where:

t – temperature, °C;
C_1', C_2 – carbon content, %.

Thus, the more supercooled the metal, the more carbon there is in the form of graphite inclusions, and the more dust is formed. As the established practice of metallurgical plants confirms, liquid iron in iron ladles cools down at a rate of 3–6 deg/h, while an open jet cools down by approximately 30 degrees in a matter of minutes [9]. During the period from the release from the blast furnace and transportation to the mixer, the temperature of the cast iron decreases by 130–180°, which naturally leads to a significant extraction of graphite from the cast iron. It was shown in [10] that graphite precipitation does not occur in the volume of cast iron but on the interfacial surfaces: exposed metal surface in the ladle, melt-ladle wall, and melt-gas bubble. When cast iron is poured into the mixer and then into the ladle, partial spraying and gas capture by the jet occurs. The resulting gas bubbles penetrate the liquid iron layer, which leads to a sharp increase in the iron-gas interface. This significantly reduces the energy of formation and growth of graphite nuclei. As a result, the number of graphite particles becomes significantly more significant, and their size is smaller than when downloading slag.

From this point of view, in the desulfurization section, the conditions for the formation and separation of graphite from cast iron are even more favorable since this process involves purging the cast iron with air, nitrogen, or rock gas (at a flow rate of up to 100 m³/h).

Various impurities in the metal have different effects on the process of graphite formation and, consequently, on dust formation. For example, Cr, Mn, S, and Mg hinder graphite formation, while Si, on the contrary, enhances this process and increases the amount of dust [4].

3. MATERIALS AND METHODS

Systematic studies of the IGW of the mixing department and the desulfurization department of the oxygen-converter shop of Azovstal Iron and Steel Works (Mariupol, Ukraine) were carried out.

For this, samples were taken (weight 2 kg) from the bins of the aspiration system. The samples were then averaged over 1 hour in a cone mixer. Next, to conduct property studies, the samples were reduced by quartering to obtain representative batches (0.5 kg). Finally, samples were taken from each batch for all subsequent analyzes and studies.

Comprehensive IGW properties studies included: a) chemical analysis; b) granulometric analysis; c) study of the microstructure; d) study of the specific volume electrical resistance, ρ_v; e) measurement of the specific saturation magnetization, σ_S.

The microstructure and morphology of IGW particles were studied using a Neophot-30 optical microscope; a REM scanning electron microscope with an X-ray analyzer and a JEM transmission electron microscope were also employed.

The differential thermal analysis method was applied to determine the temperatures of phase transformations in the studied IGW.

The magnetic properties were studied according to the procedure described in [11] using a specially made device.

To study the possibility of increasing the level of magnetic properties by their heat treatment, the installation shown in Figure 1 was used. The installation made it possible to process the material in a fixed layer and under the following modes of motion: a) a dense moving layer; b) a gravity-falling layer; c) a combined layer – gravitationally falling with subsequent movement in a dense layer.
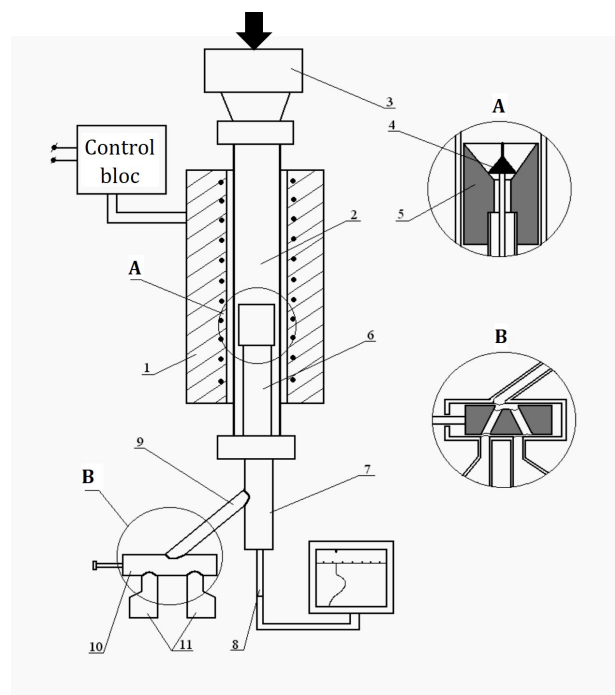
Fig. 1. The laboratory installation for heat treatment of IGW: 1 – furnace; 2 – reactor; 3 – loading device; 4 – cone; 5 – cup; 6 – tube; 7 – reactor; 8 – rod; 9 – chute; 10 – switch; 11 – material receivers

The installation consisted of an electric furnace (1) with a reactor (2) made of quartz glass. The upper part of the reactor was connected to the loading device (3), which allowed it to load dispersed IGW into the reactor without breaking the tightness. A graphite cup (5) with a cone (4) were installed in

the reactor to accumulate the material. The shutter was fixed on a tube (6), transporting the sample to the receiver. With the help of the rod (8), it was possible to move the shutter along the reactor, thereby regulating the processing time of the material while moving along the reactor.

The lower part of reactor (7) was connected to an unloading device consisting of a chute (9), a spool-type flow direction switch (10), and material receivers (11). Depending on the position of the switch, the sample entered one or another receiver without leakage. This installation also allowed conducting experiments in a controlled CO-CO_2 atmosphere in the reactor.

4. EXPERIMENTAL RESULTS AND DISCUSSION

4.1. Chemical composition

In the study of the chemical composition of dispersed IGW, the content of Fe_{met}, FeO, Fe_2O_3, C, and impurities was determined. Figure 2 shows the averaged data on the chemical composition of the IGW of the mixing department and of the desulfurization department.

a)

b)

Fig. 2. The average chemical composition [%] of dispersed IGW of the desulfurization (a) and mixing (b) departments, based on [12]

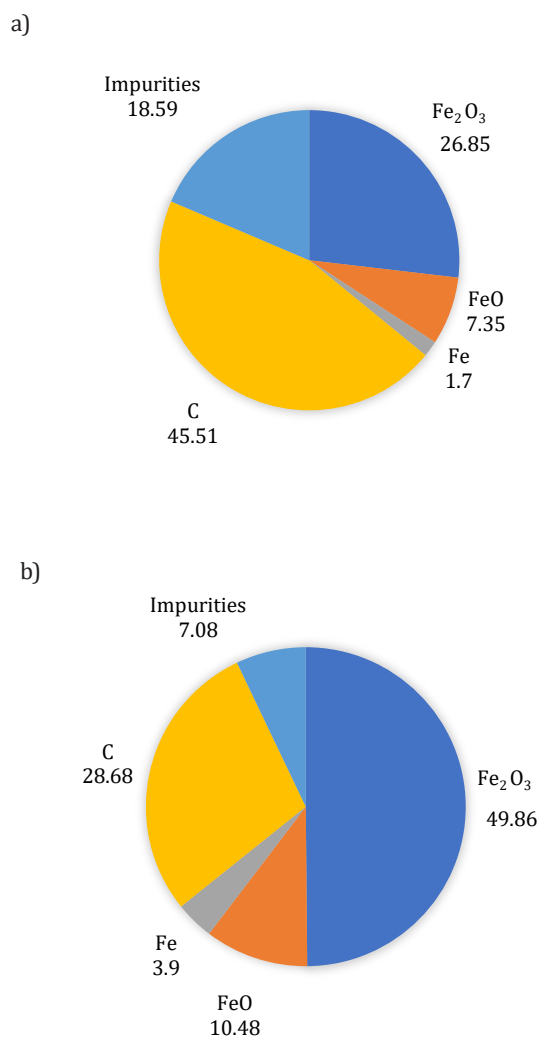As shown in Figure 2, the most typical results of the chemical analysis of the initial dispersed IGW show that the composition of these wastes depends significantly on the sampling place. For example, lower carbon content is observed in samples of the mixing department (average value – 28.68%, minimum – 14.56%, maximum – 38.44%) compared with samples of the desulfurization departments. At the same time, a higher content of iron oxides is observed (FeO, respectively, average, minimum and maximum values: 10.48, 7.57, and 15.16%; for Fe_2O_3, respectively: 49.86, 34.07, and 70.98%). Almost all of the samples contain a small amount of metallic iron, which enters the dispersed IGW in the form of tiny splashes of cast iron when poured into a mixer or a ladle (for samples from the mixing department: 3.9, 0.79 and 9.32%, respectively).

As shown, dispersed IGW in the desulfurization department is formed under somewhat different conditions, namely, when liquid iron is blown with an inert gas and magnesium powder. In this case, the cooling rate of liquid iron is greater than in the previous case, and consequently, the release of graphite is more intense. Dispersed IGW of the desulfurization department contain more carbon (average value 45.51%, minimum – 36.15%, maximum – 53.23%). According to metallic iron content, these two types of waste are close, but for the mixing department, the upper limit of the Fe_{met} content is significantly higher than for the desulfurization department (respectively, 1.7, 0.0, and 4.73%). The content of oxides for the desulfurization department IGW is less than for the mixing department (FeO, respectively, the average, minimum and maximum values: 7.35, 5.38, and 12.35%; for Fe_2O_3, respectively: 26.85, 15.51 and 34.03%).

4.2. Particle size distribution

The results of the sieve analysis of the samples of the mixing department IGW and the desulfurization department show that the central part of the material has a fineness of less than 400 μm (Fig. 3). Furthermore, a comparison of the averaged curves for the desulfurization department and the mixer department showed that the regularities of the distribution of IGW particles by fractions are universal for all the studied samples.
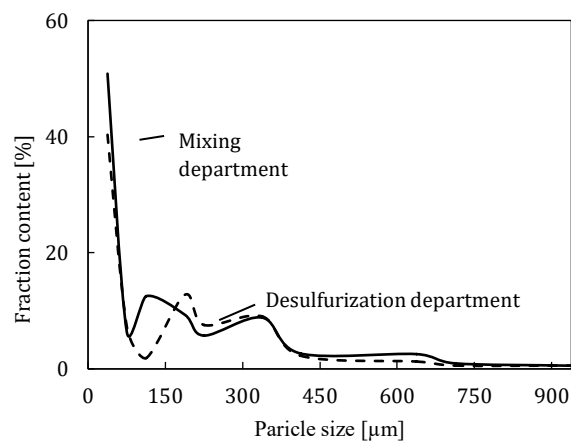

Fig. 3. Size distribution of IGW particles

Tables 1 and 2 show, by way of examples, the content of the components in various fractions of IGW for a sample from the desulfurization department. An analysis of the distribution of the main components of IGW by fractions showed the following: with a decrease in particle size, the carbon content decreases from 85% for a fraction of (−1000 +200) μm to 7.3% for a fraction of less than 50 μm. The material remaining on the sieve is marked with a plus (+) sign, and the material that has passed through the sieve is marked with a minus (−) sign. The content of FeO increases from 3.12% for the fraction (−1000 +200) μm to 16.02% for the fraction (−100 +63) μm. For the fraction −50 μm, the content of FeO is 15.46%. The content of Fe_2O_3 increased monotonically with decreasing particle size from 4% for the fraction (−1000 +200) μm to 63.3% for the fraction less than 50 μm. The amount of Fe_3O_4 with decreasing particle size increased from 11% for the fraction (−200 +160) μm to 42% for the fraction less than 50 μm.

Table 1
The main components content of the IGW depending on its dispersion (desulphurization department)

Fraction size [μm]	Chemical composition [%]				
	C	Fe_Σ	$Fe_{met.}$	FeO	Fe_2O_3
Polydisperse material	53.35	29.03	4.73	9.70	23.90
+1000	87.50	3.15	3.15	–	–
−1000 +200	85.00	8.00	2.76	3.12	4.0
−200 +160	74.00	10.74	5.52	6.85	–
−160 +100	71.23	15.00	5.50	7.00	5.70
−100 +63	48.50	31.63	13.80	16.02	7.61
−63 +50	28.50	41.03	10.65	5.30	37.50
−50	7.30	60.25	3.95	15.46	63.30

Table 2
Impurity content of the IGW depending on its dispersion (desulphurization department)

Fraction size [μm]	Chemical composition [%]						
	SiO_2	Al_2O_3	CaO	MgO	MnO	P_2O_5	S
Polydisperse material	2.10	1.10	2.90	1.00	0.90	0.474	0.231
+1000	0.72	1.01	1.86	0.22	0.90	0.948	0.112
−1000 +200	0.80	1.10	2.00	0.45	1.10	0.474	0.155
−200 +160	3.12	1.16	3.72	0.90	1.29	0.379	0.320
−160 +100	4.00	1.10	3.50	1.39	1.00	0.758	0.369
−100 +63	4.00	1.45	3.41	1.79	0.90	0.568	0.369
−63 +50	3.90	1.40	3.20	2.01	1.05	0.568	0.330
−50	2.40	0.90	3.00	1.20	1.05	0.474	0.129

4.3. Morphology and microstructure of the initial dispersed IGW particles

Figure 4 shows a general view of a layer of graphite particles and elements of the surface of a graphite plate of the IGW obtained on a scanning electron microscope. Point formations are visible on the surface of the particle. Their number corresponds to the carbon content in the IGW sample.

Increasing the magnification made it possible to detail these formations. At the same time, it was possible to determine the diameter of spherical oxide formations (from 1–5 to 25–35 µm). The level of the magnetic properties of the dispersed IGW is closely related to the amount of oxide inclusions on the surface of a graphite plates.

The use of a transmission electron microscope made it possible to establish the nature of the mutual distribution of graphite and oxide particles (Fig. 5). On Figure 5a traces of delamination of the end face of the graphite plate are visible.

There are spherical oxide particles in the protruding graphite element. They have a diameter of 250–2200 Å. Oxide particles are firmly connected with graphite, some are completely in the body of the graphite plate.

Figure 5b shows the formation of oxide particles located on the surface of a graphite plate, in which a large particle with a diameter of 1.45 µm is tightly connected to a smaller one, having a diameter of 0.43 µm. Even smaller particles are also visible, covering the surface of a larger one with a diameter of 10 to 100 nm.

The structure of the oxide particle shown in Figure 6a is also characteristic. The particle is a dense formation with a diameter of 160–170 µm, consisting of sintered smaller particles. From the outside, the shell of the particle resembles an "orange peel" type structure. The internal volume is filled with minor oxide spherical particles with a diameter of 2–10 µm. Small particles 2–7 µm in diameter are visible on the outer the surface of this large spherical object.
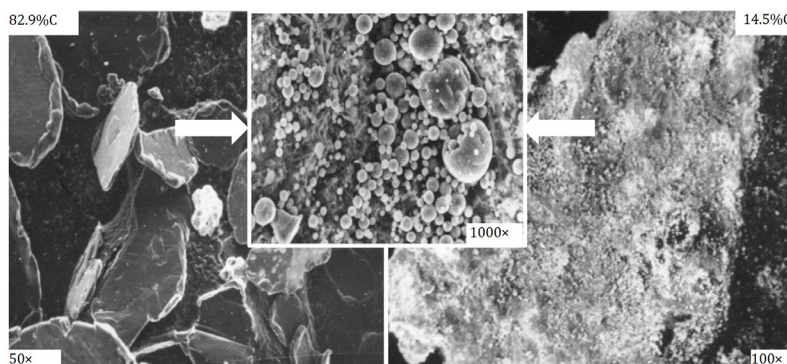

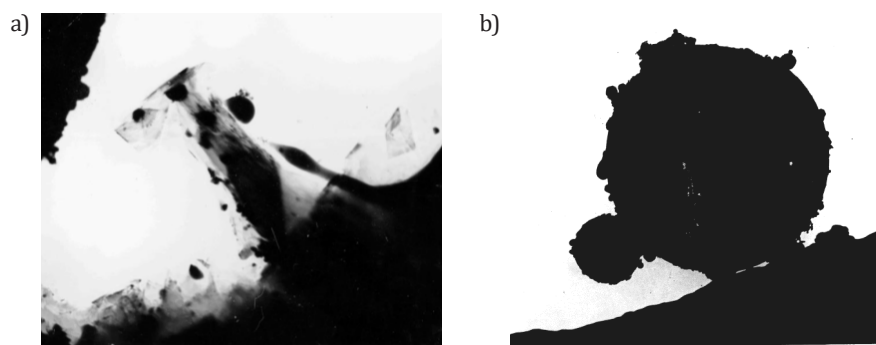**Fig. 4.** Microstructure of the graphite plate surface, based on [13]

Fig. 5. Fragments of the surface of IGW graphite plates: a) graphite plate end; b) graphite plate surface, based on [13] 40 000×
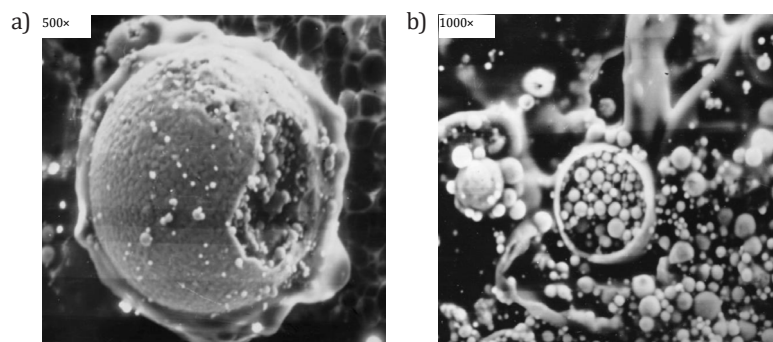

Fig. 6. . Structure of oxide particles: a) "orange peel" type structure; b) sample preliminarily subjected to pressure treatment, based on [13]

Additional information about the structure of the oxide particles of IGW is provided by the study of IGW samples preliminarily subjected to pressure treatment (in this case, a sample of the studied material was scattered on a matrix plate, and pressure was applied from above with a punch). The fracture structure (Fig. 6b) indicates that in some cases the particle is a shell filled with spherical oxide inclusions from 1 to 10 μm in diameter.

So, the study of the morphology of the initial dispersed IGW showed that they are graphite particles, the surface of which is covered to a greater or lesser extent by oxide inclusions having a complex structure. In one case, these are particles primarily of smelting origin representing dense oxide formations. In another case, these are particles that are a conglomerate of intergrown particles of smaller size, which were longer in the high-temperature zone, and this led to their strong diffusion intergrowth.

Graphite particles had a lamellar elongated shape with a thickness from 3–4 to 80 μm a characteristic luster and a layered structure. In the vast majority of particles, there were inclusions of metal directly into the body of graphite plates (Fig. 7).
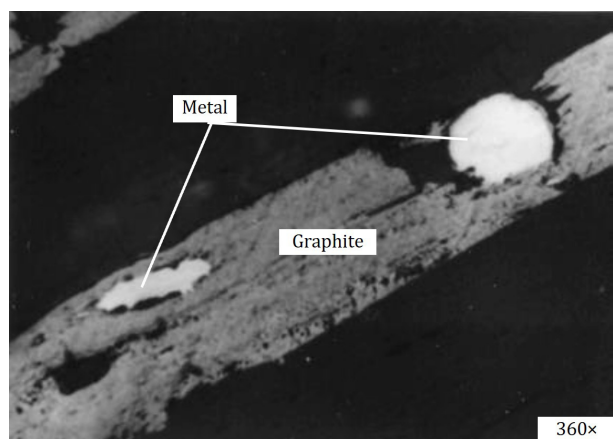

Fig. 7. Microstructure of IGW graphite particles, based on [13]

The microstructure of metal particles is carbide plates with colonies of ledeburite. This is due to the high cooling rates of metal particles in the gas flow that captured them during dispersion.

4.4. Electrical and physical properties

The specific saturation magnetization (σ_s) and electrical resistivity (ρ_v) are the most critical electrophysical properties of dispersed IGW. Therefore, the analysis of these properties of the studied materials was carried out depending on various parameters.

It is known from the literature [14–16] that dispersed IGW have magnetic properties. However, they vary widely (σ_s = 22–45 A·m²/kg).

Figure 8 shows the relationship between the granulometric composition of dispersed IGW and its magnetic properties. In the experiment, it was found that with a decrease in the dispersion of the material, the value of σ_s increases and

reaches a maximum for the tiniest fractions. The maximum of σ_s with a simultaneous minimum of Fe$_{met.}$ (Tab. 1) makes possible the conclusion that the oxide magnetic component plays a dominant role in the magnitude of the magnetic properties. Dispersed IGW, as a rule, have a very low electrical resistivity – (4.18–0.46)·10^{-4} ohm·m [16]. Since dispersed IGW are polydisperse, a study was made of the effect of the dispersed composition on the specific electrical resistance. The ρ_v of the starting material is 2.41·10^{-4} ohm·m. The results of measuring ρ_v of individual fractions are shown in Figure 9. For ease of perception, the dependence of ρ_v on the particle size in Figure 9 was built in semi-logarithmic coordinates.
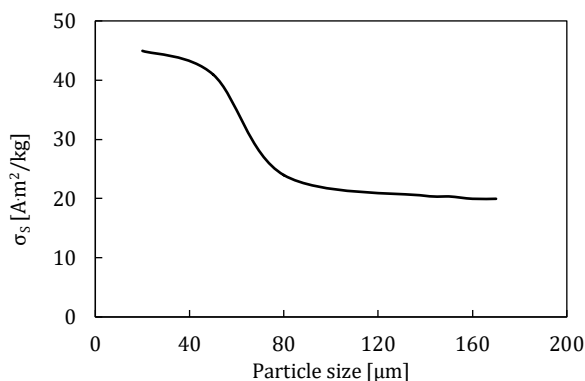
Fig. 8. Dependence of the magnetic properties of dispersed IGW on the granulometric composition
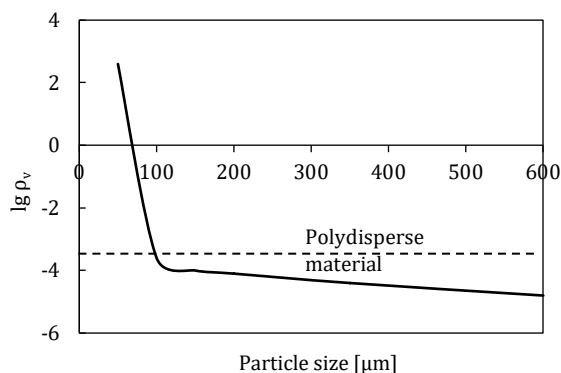
Fig. 9. Specific electrical resistance of IGW depending on their dispersion

Analysis of the graph shows that in the range from 600 μm to 200 μm, the value of ρ_v is minimal and lies within (2.06–2.53)·10^{-4} ohm·m. In the dispersity range of 200–63 μm, an increase in ρ_v from 2.25·10^{-4} to 6.0·10^{-4} ohm·m is observed with a decrease in particle size, which is due to a decrease in the carbon content from 28.0 to 8–15%. A further decrease in dispersion leads to an even greater decrease in the carbon content. As a result, already for a dispersion of 50–63 μm, the value of ρ_v is 0.15·10^{-2} ohm·m, and for a dispersion of less than 50 μm, the value of ρ_v becomes equal to ~5·10³ ohm·m. Thus, the value of ρ_v, depending on the disperse composition, can vary by almost six orders of magnitude.

4.5. Differential thermal analysis of IGW

The chemical composition and morphology of dispersed IGW in the context of their magnetic properties showed that the

material has excellent potential for these properties. An increase in the content of magnetic components (metallic iron and Fe_3O_4 oxide) in IGW is possible due to carbothermal self-reduction in the first case and magnetizing annealing in the second.

When studying reduction processes in new systems, it is essential to determine the temperatures at which the interaction begins [17]. For this purpose, a differential thermal analysis (DTA) of the studied dispersed IGW was carried out.

DTA was carried out stepwise: heating at a rate of 10 degrees per minute to a temperature of 850°C and then at a rate of 2 degrees per minute.

The results obtained show that there are three segments on the DTA curve. The first endoeffect was observed at temperatures of 60–200°C. In this case, condensation of water droplets was observed on the cold parts of the reactor with the sample. Thus, the first peak of the endoeffect corresponded to the removal of hygroscopic moisture from the sample.

The endoeffect was observed at 500–850°C, a more petite height but extended in time. At the same time, a slight gas evolution occurred in the reactor.

An additional experiment carried out at 900°C, and a long exposure showed that a non-magnetic material is obtained at this temperature, i.e., all iron oxides are converted to wustite. Consequently, the peaks corresponding to the reduction of hematite and magnetite on the thermogram merge into one peak. This was due to the high heating rate at this analysis stage.

The third peak of the endoeffect began at 960 ±5°C and was accompanied by the greatest of the endoeffects. From this moment, intensive gas evolution began. This DTA peak is a consequence of the endoeffect of reduction of wustite by the graphite. With an increase in temperature, the intensity of gas evolution increased, and the magnitude of the endoeffect grew. The limiting temperature during thermographic studies was 1000°C.

The analysis of the obtained results showed that the magnetizing treatment of dispersed IGW should be carried out in the temperature range of 600–700°C and metallization – at temperatures above 980°C.

4.6. High-temperature treatment of dispersed IGW

Magnetizing annealing

The conditions for carrying out the technological process of high-temperature treatment of dispersed IGW determine the quantitative characteristics of the process, as well as the parameters of the resulting product. In this regard, the following options for the implementation of magnetizing annealing and carbothermal self-reduction were investigated in this work: a) in a dense fixed layer; b) in a dense vertically moving layer; c) in a combined (gravitationally falling and following a dense moving) layer.

When choosing the operating temperature range, we were guided both by the DTA results and by the course of the curves on the Fe-O-C equilibrium diagram. The lower temperature limit at which magnetite becomes a thermodynamically probable phase is 570°C. At temperatures above 650°C, wustite becomes more thermodynamically probable [18–21].

According to [22], in the case of carbon content in ores of more than 0.1%, it is sufficient to heat the ore to 570–660°C to carry out magnetizing annealing without using a reducing agent. Moreover, if it is necessary to use the reducing effect of the carbon in the ore, then the ore heating in the furnace is recommended to be carried out in a neutral atmosphere or without air access. Solid carbon reduces the ore only at a temperature of approximately 650°C [22, 23]. Based on this brief analysis, the following temperatures were chosen for the experiments: 600, 650, and 700°C.

The presence of such an amount of carbon in the material and oxygen in the reactor of the installation provided the necessary CO-CO_2 atmosphere for the reduction reactions to proceed in full. The material was heated and processed in a reactor (Fig. 1) without air access, i.e., in its atmosphere. The obtained results were analyzed only for the period of isothermal exposure to the material. During the experiments, the σ_s of the final product was controlled. Figure 10 shows the kinetic curves of the magnetizing annealing of these samples. At a process temperature of 600°C, an increase in the value of σ_s was observed with an increase in the isothermal holding time from 0 to 90 min, but the process was especially intensive in the first 10 min. The maximum value of σ_s was obtained only after 90 min of the experiment (75 min of exposure at a constant temperature) and amounted to 87 A·m²/kg (or 94.5% of the maximum possible value corresponding to the content of 100% magnetite).
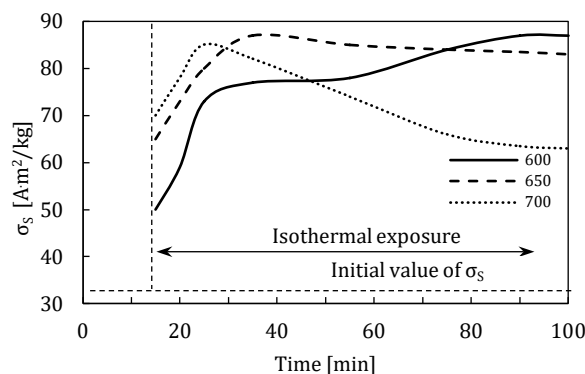
Fig. 10. Kinetics of magnetizing annealing of IGW in a dense fixed layer, based on [24]

Increasing the temperature to 650°C led to the intensification of the process. Thus, after 20 min of exposure at a constant temperature, the value of σ_s reached 87 A·m²/kg.

With a long exposure, the gas medium should approach equilibrium by the Fe-O-C diagram. According to this diagram, at temperatures above 650°C, the gas phase corresponds to the stable state of wustite. However, the process of magnetite formation is faster than its reduction to wustite. Therefore, at temperatures above 650°C, at first, most of the oxides are converted into magnetite, and with an increase in its amount, reduction to wustite begins. This explains the course of the curve at 700°C in Figure 10. From a technological point of view, the moving layer is more attractive than the fixed one. In experiments on magnetizing annealing in a dense moving layer, the speed of material movement through the reactor was 5, 10, 20, and 40 mm/min. At the

same time, the residence time of the material in the thermo-stable zone with a temperature of 650°C was 80, 40, 20 and 10 min, respectively.

Figure 11 shows the kinetic curve of the magnetizing annealing of the IGW in a dense moving layer. As in previous experiments, it was enough to keep the material at 650°C for 35 min to obtain 95% of magnetite from the maximum possible amount. This corresponded to the speed of movement of the material through the reactor, 10 mm/min.
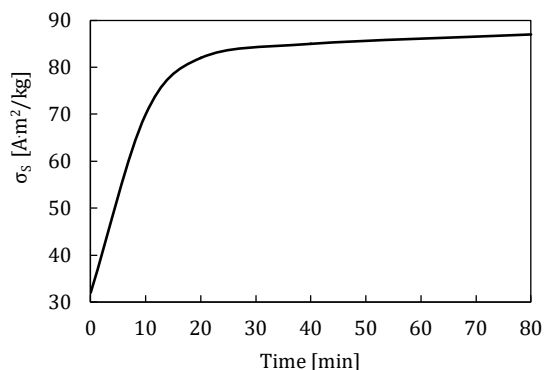

Fig. 11. Kinetics of magnetizing annealing of IGW at 650°C in a dense moving layer

The experiments have shown that obtaining high values of σ_s is associated with a long processing time. The link limiting the performance of the reactor is the rate of heating of the processed material to the operating temperature. A dense layer of IGW can be identified with a quasi-monolithic body, which has low thermal conductivity and warms up slowly. On the other hand, it is known that in the mode of a gravitation-ally falling layer, very high heat transfer coefficients can be obtained – up to 3000 W/(m²·K) [25].

The features of the gravitationally falling layer are as follows:

1) particles entering the reactor are in a state independent of each other and begin to move only under the action of gravitational force. When their movement conditions are met, heating, chemical, and structural transformations will be equivalent. In this case, the powder particles are accelerated to a speed equal to or close to the speed of hovering relative to the reagent gas. Heating and all transformations are thus carried out in the process of falling particles;

2) the distance between the particles significantly exceeds their diameter;

3) each particle is in an equiprobable state from the point of view of flow by the reagent gas and interaction with it.

Studies of the magnetizing annealing of dispersed IGW in their atmosphere (IGW carbon content – 10%) in the mode of a gravitationally falling layer, followed by exposure in a dense layer, were carried out on an installation, the scheme of which is shown in Figure 1. In the gravitational falling layer mode, the material passed through the non-isothermal zone of the reactor, was heated to the operating temperature, and then accumulated in the isothermal zone. The temperature in this reactor zone was set in the range from 600 to 800°C.

It was found that already after 2 seconds of movement in the falling layer mode, the saturation-specific magnetization increased from 32 to 47 A·m²/kg at a reactor temperature of 600°C, to 62 A·m²/kg at a reactor temperature of 650°C, to 70 A·m²/kg at a reactor temperature of 700°C and up to 75 A·m²/kg at a reactor temperature of 800°C.

Further exposure for 100 min at a temperature of 600°C led to a monotonic increase in the value of σ_s up to 87 A·m²/kg. This indicated the transition of almost all iron oxides contained in the samples to magnetite.

The process of magnetizing annealing at higher tempera-tures in a dense layer proceeded very quickly: at 800°C, an increase in the value of σ_s to 87 A·m²/kg was observed already after 2–3 min from the start of treatment, and at 700°C, after 7–8 min. Then, by the Fe-O-CO-CO₂ diagram, the transforma-tion of the formed magnetite into the nonmagnetic oxide FeO began. This led to a decrease in the sample's magnetic proper-ties to 60 A·m²/kg after 100 min exposure.

On the basis of the results obtained, it was proposed to preheat the initial dispersed IGW in the gravitational-falling layer mode before magnetizing annealing in the dense layer mode. Considering in addition to technological and economic aspects, the optimal temperature in the reactor should be rec-ognized as 700°C.

Carbothermal self-reduction

Both magnetite and metallic iron can ensure the high mag-netic properties of iron-graphite waste after high-tempera-ture treatment. The process leading to the reduction of all iron oxides of IGW to metallic iron by the carbon contained in the material itself is, in fact, the process of carbothermal self-reduction (CTSR).

The studies were carried out on polydisperse samples of IGW with a fraction of fewer than 400 μm. The samples con-tained 38% C and ~40% Fe$_\Sigma$. In the experiments, the samples were heated in a dense fixed layer to 1000, 1025, and 1090°C. In the process, the degree of reduction, α, was determined.

Curves characterizing the kinetics of the process of CTSR of IGW to metallic iron (metallization) at given temperatures are shown in Figure 12.
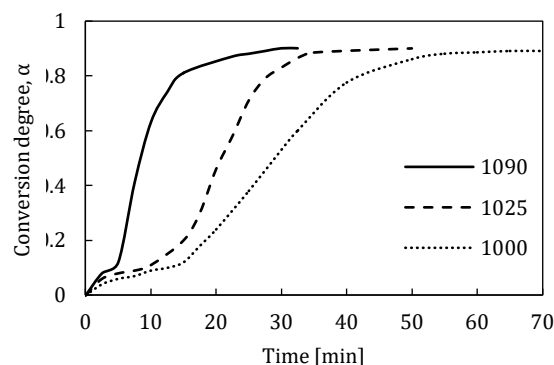

Fig. 12. Kinetics of CTSR of IGW in a dense fixed layer, based on [26]

It can be seen from the figure that the temperature sig-nificantly affects the total duration of reduction up to the value α equal to 0.9 (σ_s = 180 A·m²/kg). The temperature increasing from 1000 to 1090°C reduces the processing time

from 70 to 30 min, i.e. 2.33 times. The shape of the curves indicates a two-stage reduction process. It is thermodynamically apparent that the reduction of higher iron oxides to wustite took place in the first stage, and the process of metallization took place in the second stage. Both stages began very quickly in this case, then the process slowed (Fig. 12).

Consideration of each step of the process from the point of view of topokinetic theory made it possible to explain the course of the curves in Figure 12.

It is known that if a chemical process proceeds with the participation of different phases, the reaction occurs at their interface [27, 28]. Therefore, the process studied in this work is topochemical. Modern topochemistry considers such processes as two-stage ones [29]. The first stage of interaction between a gas and a solid consists of forming product nuclei on the surface of a solid reagent, their growth, and coalescence. In the second stage, a continuous thin shell of the product is formed on the entire reaction surface, followed by the advance of the reaction front deep into the solid reagent. In this case, the process rate decreases under the influence of two factors: a decrease in the reaction surface and an increase in the effect of diffusion resistance due to the layer of the solid product thickness increasing. In the study of processes in the combined mode of motion, a sample of dispersed IGW was heated in a gravitationally falling layer, then in a dense layer, iron oxides were reduced by the carbon of the sample. As in the case of magnetizing annealing, preheating of the material in the mode of a gravitationally falling layer significantly accelerated the process. Thus, at a temperature in the isothermal zone of 1090°C, the metallization process was completed by ~90% after 24 min, at a temperature of 1025°C – after 28, and at 1000°C – after 50 min, i.e. flowed approximately 1.23 times faster than in the dense layer regime.

4.7. General technological scheme of dispersed IGW processing

The complex studies conducted on the physicochemical, electrophysical, and technological properties, as well as their morphology and microstructure, allows us to consider dispersed IGW of metallurgical production as a promising raw material for creating composite materials with radio-absorbing and radio-shielding properties. This follows from the considerations below.

To create effective composite materials that absorb microwave radiation, it is necessary to be guided by physical and electrophysical concepts in combination with a physicochemical approach to finding optimal compositions. At the same time, a thorough analysis shows that one of the most promising ways is using heterogeneous two- or more-component materials.

The first essential physicochemical condition for the most efficient absorption of materials of the metal (oxide) – dielectric type of microwave radiation is the following: maximum absorption is achieved if the dimensions of the metal component are one order of magnitude or not more than one order of magnitude greater than the value of the skin layer, and a component with dielectric properties completely insulates a metal component evenly distributed over the volume.

The second physicochemical condition for creating materials that absorb microwave radiation is using such components with high structure stability, composition, and properties under thermal, corrosion, and other influences.

Based on these prerequisites and the generalization of the results obtained in laboratory studies, a general scheme of dispersed IGW complex processing was developed (Fig. 13). Considering the heterogeneity of IGW from various sources, both in terms of chemical and granulometric composition, in accordance with the proposed scheme, the waste should be subjected to screening, grinding, and averaging.

Based on the fact that the central part of iron oxides is contained in a fraction of less than 160 μm, and the main proportion of graphite is in a fraction of more than 160 μm (Tab. 1), it is proposed to divide the IGW into two fractions: +160 and –160 μm.

At the same time, the +160 μm fraction of IGW can be used directly without further processing, for example, as a raw material for graphite extraction. The –160 μm fraction has higher magnetic properties and can be used as a starting material for further high-temperature processing to increase the level of these properties. Stabilization of the properties of the starting material and the final product is ensured by averaging.

In order to obtain a fraction of IGW less than 50 μm, the technological scheme provides for a grinding operation, after which the resulting material (−50 μm) is also sent to an average.

An increase in the magnetic properties of iron-graphite waste is associated with the screening of a large fraction and with the implementation of high-temperature processing.
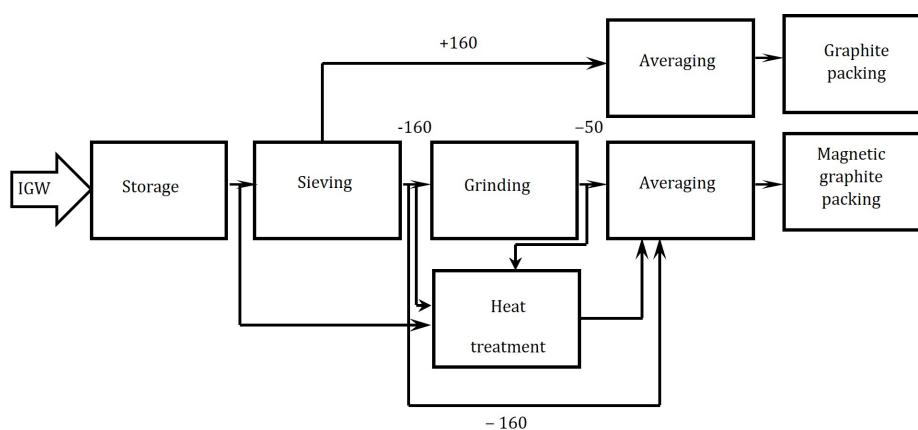

Fig. 13. General scheme of dispersed IGW complex processing, based on [30]

This treatment is the most effective method of increasing the magnetic properties of the starting material and can be done in two ways. The first way is magnetizing annealing, the maximum possible amount of magnetite (Fe_3O_4) in the IGW.

The resulting material can be positioned as "Magnetized magnetic graphite." The second way is reduction processing to metallic iron by carbothermic self-reducing. The resulting material can be characterized as "Metallized magnetic graphite". According to the technological scheme, high-temperature processing can be subjected to both the initial IGW and the product after sieving and milling.

The finished product must have a given level of magnetic and electrical properties. Therefore, the technological scheme provides for averaging the magnetic material's composition.

Thus, a technological scheme with many bonds will make it possible to obtain magnetic graphite with different electrical properties and a practically non-magnetic material containing a large amount of graphite.

The proposed technological scheme was implemented at the Markograph plant (Mariupol, Ukraine) by designing and building a workshop. As a result, fifteen tons of magnetic graphite were produced. Furthermore, from this amount of graphite, 25 tons of composite materials and products for lining rooms with equipment emitting in the microwave range and intended for storing information on electronic media were produced.

An industry standard for magnetic graphite (TU U 02070812.002) was developed.

5. CONCLUSIONS

In this research work, a systematic analysis of the conditions for the formation, structure, and properties of dispersed iron-graphite wastes of metallurgical production was carried out, and ways of their complex utilization were determined. The following was established:

1. The principal amount of dispersed iron-graphite waste at metallurgical enterprises is formed in the desulfurization and mixing departments. Depending on the place of formation, iron-graphite waste contains in its composition a different amount of the main components: carbon, metallic iron, iron oxides, and impurities.
2. Iron-graphite waste is polydisperse. The main number of particles has a size of fewer than 400 microns. The components are unevenly distributed in different fractions of the material. The carbon content decreases from 85% for the fraction (−1000 +200) μm to 7.3% for the fraction less than 50 μm. On the contrary, the total content of iron oxides increases from 7.12% for the fraction (−1000 +200) μm to 78.76% for the fraction less than 50 μm.
3. An analysis of the morphology and microstructure of IGW showed that graphite particles are scaly in shape; iron oxide particles are spherical, a significant part of them are mechanically bonded to graphite, and several particles are even inside graphite flakes.
4. The presence of oxide and metal particles on the surface and inside the graphite plates explains the presence of magnetic properties in iron-graphite waste. At the same time, it was found that the specific saturation magnetization varies depending on the particle size of the material: it increases from 20 A·m^2/kg for a fraction of 200 μm to 50 A·m^2/kg for a fraction of less than 50 μm. The effect of material fineness on the electrical resistivity was also found: ρ_v increases from $(2{-}6) \cdot 10^{-4}$ ohm·m for particles larger than 200 μm to $5 \cdot 10^3$ ohm·m for particles smaller than 50 μm.
5. Using differential thermal analysis, studies of the temperature conditions for the interaction of iron oxides and graphite in dispersed IGW were carried out. The possibility of magnetizing annealing at 600–700°C and carbothermal self-reduction at temperatures above 980°C has been established.
6. On the basis of studies of the kinetic regularities of magnetizing annealing at various temperatures and modes of motion, the conditions for an almost complete magnetic transformation in dispersed IGW have been established. At a temperature of 650°C, in the combined mode of motion, a material with high electrophysical properties is obtained already in 7 min (σ_s = 87 A·m^2/kg, $\rho_v \sim 10^{-4}$ ohm·m).
7. The possibility of obtaining a material with a high specific saturation magnetization (σ_s = 180 A·m^2/kg, with a low specific electrical resistance $\rho_v \sim 2 \cdot 10^{-4}$ ohm·m) from dispersed IGW was established by carbothermal self-reduction at a temperature of 1090°C in a combined layer in 24 min.
8. A technological scheme of dispersed IGW processing was proposed and implemented. It provided for two products to be obtained: graphite and magnetic graphite with a given level of electrical and magnetic properties. Tests of magnetic graphite showed its high efficiency both as an independent protective material and as a component of a composite protective material against microwave radiation.

REFERENCES

[1] Pullin H., Bray A.W., Burke I.T., Muir D.D., Sapsford D.J., Mayes W.M. & Renforth P. (2019). Atmospheric Carbon Capture Performance of Legacy Iron and Steel Waste. *Environmental Science & Technology*, 53 (16), 9502–9511. Doi: https://doi.org/10.1021/acs.est.9b01265.

[2] Gurov N.I. & Fedotov A.A. (1982). Opredeleniye ob"yema resursov grafita v grafitosoderzhashchikh otkhodakh metallurgicheskikh zavodov i effektivnost' ikh ispol'zovaniya. *Stal'*, 11, 16–18 [Гуров Н.И., Федотов А.А. (1982). Определение объема ресурсов графита в графитосодержащих отходах металлургических заводов и эффективность их использования. *Сталь*, 11, 16–18].

[3] Fadeyeva N.V., Orekhova N.N. & Gorlova O.Ye. (2019). Opyt pererabotki grafitsoderzhashchey pyli metallurgicheskogo proizvodstva. *Chernaya metallurgiya. Byulleten' nauchno-tekhnicheskoy i ekonomicheskoy informatsii*, 7(5), 632–639. Doi: https://doi.org/10.32339/0135-5910-2019-5-632-639 [Фадеева Н.В., Орехова Н.Н., Горлова О.Е. (2019). Опыт переработки графитсодержащей пыли металлургического производства. *Черная металлургия. Бюллетень научнотехнической и экономической информации*, 7(5), 632–639].

[4] Tolochko A.I., Slavin V.I., Suprun YU.M. & Khayrutdinov R.M. (1990). *Utilizatsiya pyley i shlamov v chernoy metallurgii.* Chelyabinsk: Metallurgiya [Толочко А.И., Славин В.И., Супрун Ю.М., Хайрутдинов Р.М. (1990). *Утилизация пылей и шламов в черной металлургии.* Челябинск: Металлургия].

[5] Laverty P.D., Nicks L.J. & Walters L.A. (1994). *Recovery of Flake Graphite From Steelmaking Kish. Report of Investigations 9512.* Reno: United States Department of the Interior Bureau of Mines.

[6] Ozhogin V.V., Tomash A.A. & Chernova S.G. (2003). Polucheniye vysokozakisnogo martenovskogo aglomerata iz otkhodov. *10-ya nauchno-tekhnicheskaya konferentsiya 20–23 maya 2003, Mariupol',* Ukraina, 12–13. Mariupol': Izdatel'stvo PGTU [Ожогин В.В., Томаш А.А., Чернова С.Г. (2003). Получение высококозакисного мартеновского агломерата из отходов. *10-я научно-техническая конференция 20–23 мая 2003,* Мариуполь, Украина, 12–13. Мариуполь: Издательство ПГТУ].

[7] Kravets' V.A. (2018). Doslidzhennya vlastyvostey metalurhiynoho hrafitu z metoyu podal'shoyi utylizatsiyi. *Zbirnyk naukovykh prats' Donbas'koyi natsional'noyi akademiyi budivnytstva i arkhitektury,* 11(1), 38–52. Retrieved from: http://nbuv.gov.ua/UJRN/zbnpd-naba_2018_1_8 [accessed 26.09.2022] [Кравець В.А. (2018). Дослідження властивостей металургійного графіту з метою подальшої утилізації. *Збірник наукових праць Донбаської національної академії будівництва і архітектури,* 11(1), 38–52].

[8] Vertman A.A. & Samarin A.M. (1969). *Svoystva rasplavov zheleza.* Moskva: Nauka [Вертман А.А., Самарин А.М. (1969). *Свойства расплавов железа.* Москва: Наука].

[9] D'yachko Yu.P. & Shaynovich O.I. (1970). Sravneniye razlichnykh skhem podachi zhidkogo chuguna v staleplavil'nyye pechi. *Stal',* 7, 650–654 [Дьячко Ю.П., Шайнович О.И. (1970). Сравнение различных схем подачи жидкого чугуна в сталеплавильные печи. *Сталь,* 7, 650–654].

[10] Zakharchenko E.V. & Loper K.D. (1981). *Ginezis i morfologiya spelevogo grafita v chugune domennoy plavki. Novoye v metallografii chuguna.* Kiyev: IPL AN USSR [Захарченко Э.В., Лопер К.Д. (1981). *Гинезис и морфология спелевого графита в чугуне доменной плавки. Новое в металлографии чугуна.* Киев: ИПЛ АН УССР].

[11] Tul'chinskiy L.N. (1984). Osobennosti magnitnykh izmereniy poroshkov. In: Tul'chinskiy L.N. (Ed.), *Poroshkovyye magnitnyye materialy.* Kiyev: IPM AN USSR, 117–127 [Тульчинский Л.Н. (1984). Особенности магнитных измерений порошков. В Тульчинский Л.Н., *Порошковые магнитные материалы.* Киев: ИПМ АН УССР, 117–127].

[12] Maslov V.A., Trofimova L.A. & Dan L.A. (2015). Sravneniye fiziko-khimicheskikh svoystv dispersnykh ZHGO miksernogo otdeleniya i otdeleniya desul'furatsii. Teplo- i massoobmennyye protsessy v metallurgicheskikh sistemakh. Materialy IX Mezhdunarodnoy nauchno-tekhnicheskoy konferentsii, Mariupol', Ukraina 9–11 sentyabrya 2015 g. Mariupol': Izdatel'stvo PGTU, 151–155 [Маслов В.А., Трофимова Л.А., Дан Л.А. (2015). Сравнение физико-химических свойств дисперсных ЖГО миксерного отделения и отделения десульфурации. Тепло- и массообменные процессы в металлургических системах. Материалы IX Международной научно-технической конференции, Мариуполь, Украина 9–11 сентября 2015 г. Мариуполь: Издательство ПГТУ, 151–155].

[13] Maslov V.A., Trofimova L.A. & Dan L.A. (2009). Structural-Morphological and Electrophysical Characteristics of Disperse Iron–Graphite Metallurgical Wastes. *Steel in Translation,* 9(7), 551–555. Doi: https://doi.org/10.3103/S0967091209070080.

[14] Shuya Li, Bo Zhang, Di Wu, Zhiwei Li, Sheng-Qi Chu, Xiang Ding, Xingfu Tang, Jianmin Chen & Qing Li (2021) Magnetic Particles Unintentionally Emitted from Anthropogenic Sources. Iron and Steel Plants. *Environmental Science & Technology Letters,* 8, 295–300. Doi: https://doi.org/10.1021/acs.estlett.1c00164.

[15] Michalik J.M., Wilczyńska-Michalik W., Gondek Ł., Tokarz W., Żukrowski J., Gajewska M. & Michalik M. (2022). *Magnetic fraction of the atmospheric dust in Kraków – physicochemical characteristics and possible environmental impact.* Retrieved from: https://doi.org/10.5194/egusphere-2022-462 (accessed 4.07.2022).

[16] Yuzhakov B.A. & Maslov V.A. (1998). Issledovaniye fiziko–khimicheskikh i tekhnologicheskikh svoystv dispersnykh zhelezografitovykh otkhodov OAO «Azovstal'». *Vestnik PGTU,* 6, 30–34 [Южаков Б.А., Маслов В.А. (1998). Исследование физико–химических и технологических свойств дисперсных железографитовых отходов ОАО «Азовсталь». *Вестник ПГТУ,* 6, 30–34].

[17] Berg L.G. (1969). *Vvedeniye v termografiyu.* Moskva: Nauka [Берг Л.Г. (1969). *Введение в термографию.* Москва: Наука].

[18] Shapovalov A.N. (2015). *Teoriya metallurgicheskikh protsessov.* Novotroitsk: NF NITU [Шаповалов А.Н. (2015). *Теория металлургических процессов.* Новотроицк: НФ НИТУ].

[19] Vanyukov A.V. & Zaytsev V.Ya. (1973). Teoriya pirometallurgicheskikh protsessov. Moskva: Metallurgiya [Ванюков А.В., Зайцев В.Я. (1973). *Теория пирометаллургических процессов.* Москва: Металлургия].

[20] Linchevskiy B.V. (1995). *Teoriya metallurgicheskikh protsessov.* Metallurgiya: Moskva [Линчевский Б.В. (1995). *Теория металлургических процессов.* Металлургия: Москва].

[21] Luk'yanchikov A.S. (1962). Gazovyy obzhig zheleznykh rud. Kiyev: Gosudarstvennoye izdatel'stvo tekhnicheskoy literatury [Лукьянчиков А.С. (1962). *Газовый обжиг железных руд.* Киев: Государственное издательство технической литературы].

[22] Lepilo N.N. & Shur A.B. (2000). Modelirovaniye izmeneniy pryamogo vosstanovleniya zheleza v domennoy plavke. Izvestiya VUZov. *Chernaya metallurgiya,* 3, 14–16 [Лепило Н.Н., Шур А.Б. (2000). Моделирование изменений прямого восстановления железа в доменной плавке. Известия ВУЗов. *Черная металлургия,* 3, 14–16].

[23] Zaytsev A.K., Krivolapov N.V., Valavin V.S. & Vandar'yev S.V. (2002). Osobennosti vosstanovleniya zheleza kamennougol'nymi i grafitovymi materialami iz malozhelezistogo shlaka. Izvestiya VUZov. Chernaya metallurgiya, 3, 6–15 [Зайцев А.К., Криволапов Н.В., Валавин В.С., Вандарьев С.В. (2002). Особенности восстановления железа каменноугольными и графитовыми материалами из маложелезистого шлака. Известия ВУЗов. *Черная металлургия,* 3, 6–15].

[24] Trofimova L.O. (2007). Rozrobka tekhnolohiyi vysokotemperaturnoyi pererobky dyspersnykh zalizohrafitovykh vidkhodiv metalurhiynoho vyrobnytstva. Avtoreferat dysertatsiyi na zdobuttya naukovoho stupenya kandidata tekhnichnykh nauk PDTU, Mariupol', Ukrayina [Трофімова Л.О. (2007). Розробка технології високотемпературної переробки дисперсних залізографітових відходів металургійного виробництва. Автореферат дисертації на здобуття наукового ступеня кандидата технічних наук. ПДТУ, Маріуполь, Україна].

[25] Maslov V.A., Trofimova L.A., & Dan L.A. (2006). Dinamika dvizheniya i nagreva dispersnykh zhelezografitovykh otkhodov v gravitatsionno-padayushchem sloye. *Vestnik PGTU,* 16, 1–5. [Маслов В.А., Трофимова Л.А., Дан Л.А. (2006). Динамика движения и нагрева дисперсных железографитовых отходов в гравитационно-падающем слое. *Вестник ПГТУ,* 16, 1–5].

[26] Maslov V.A. & Trofimova L.A. (2004). Issledovaniye kinetiki karbotermicheskogo samovosstanovleniya zhelezografitovykh otkhodov metallurgicheskogo proizvodstva. *Vestnik PGTU,* 14, 41–43 [Маслов В.А., Трофимова Л.А. (2004). Исследование кинетики карботермического самовосстановления железографитовых отходов металлургического производства. *Вестник ПГТУ,* 14, 41–43].

[27] Krylov O.V. (1973). Razvitiye sovremennykh predstavleniy o kinetike geterogennykh reaktsiy v rabotakh S.Z. Roginskogo. Problemy kinetiki i kataliza. XV. Mekhanizm i kinetika geterogennykh reaktsiy. Moskva: Nauka, 5–11 [Крылов О.В. (1973). Развитие современных представлений о кинетике гетерогенных реакций в работах С.З. Рогинского. Проблемы кинетики и катализа. XV. Механизм и кинетика гетерогенных реакций. Москва: Наука, 5–11].

[28] Rozovskiy A.Ya. (1974). *Kinetika topokhimicheskikh reaktsiy.* Moskva: Khimiya [Розовский А.Я. (1974). *Кинетика топохимических реакций.* Москва: Химия].

[29] Barret P. (1973). *Cinétique hétérogène.* Paris: Gauthier-Villars.

[30] Maslov V.A., Trofimova L.A. & Dan L.A. (2018). Pererabotka i utilizatsiya zhelezografitovykh otkhodov metallurgicheskogo proizvodstva. *Liteynoye proizvodstvo i metallurgiya,* 90 (1), 96–99. Doi: https://doi.org/10.21122/1683-6065-2018-1-96-99 [Маслов В.А., Трофимова Л.А., Дан Л.А. (2018). Переработка и утилизация железографитовых отходов металлургического производства. *Литейное производство и металлургия,* 90 (1), 96–99].